

Silicon isotopes in an EMIC's ocean: sensitivity to runoff, iron supply and climate

¹Institute of Geosciences, Christian-Albrechts-University of Kiel, Ludewig-Meyn-Strasse 10, 24118, Kiel,

Germany

²GEOMAR Helmholtz Centre for Ocean Research, Kiel, Düsternbrooker Weg 20, 24105, Germany

³Potsdam Institute for Climate Impact Research (PIK), Telegraphenberg A62 / 0.04, 14412 Potsdam,

Germany

⁴Institute of Marine Research, 1870 Nordnes, NO-5817, Bergen, Norway

⁵Bjerknes Centre for Climate Research, Bergen, Norway

H. Dietze^{1,2}, U. Löptien^{1,2}, R. Hordoir^{4,5}, M. Heinemann¹, W. Huiskamp³, B. Schneider¹

Key Points:

- We simulate the isotopic composition of biogenic silica archived in the ocean's sediment.
- Our simulations with an Earth System Model compare modern climate to glacial conditions.
- Out of several hypotheses tested, altering the isotopic composition of runoff during the LGM is most consistent with proxies.

Abstract

The isotopic composition of Si in biogenic silica (BSi), such as opal buried in the oceans' sediments, has changed over time. Paleo records suggest that the isotopic composition, described in terms of $\delta^{30}\text{Si}$, was generally much lower during glacial times than today. There is consensus that this variability is attributable to differing environmental conditions at the respective time of BSi production and sedimentation. The detailed links between environmental conditions and the isotopic composition of BSi in the sediments remain, however, poorly constrained. In this study, we explore the effects of a suite of offset boundary conditions during the LGM on the isotopic composition of BSi archived in sediments in an Earth System Model of intermediate complexity. Our model results suggest that a change in the isotopic composition of Si supply to the glacial ocean is sufficient to explain the observed overall low(er) glacial $\delta^{30}\text{Si}$ in BSi. All other processes explored triggered model responses of either wrong sign or magnitude, or are inconsistent with a recent estimate of bottom water oxygenation in the Atlantic Sector of the Southern Ocean. Caveats, mainly associated with generic uncertainties in today's pelagic biogeochemical modules, remain.

1 Introduction

Numerical, model-based projections into our warming future suggest ensuing global-scale redistribution of nutrients from the sun-lit surface ocean to depth. Among the prospective consequences are declining biological productivity and fish yields. Disconcertingly, these effects may prevail for a millennium (Moore et al., 2018). But how reliable are such climate projections?

The problem is that we will not live to calculate substantiated statistics on the reliability of climate forecasts. Hence, an approach similar to the one pursued in weather-forecasting, where progress has been accomplished during decades of daily forecasts and subsequent ground-truthing (c.f. Bauer et al., 2015), is not viable – if pressing societal questions are to be answered in time. A straight-forward and generic way to deal with this problem is to assume that fidelity of now-casts is correlated with the fidelity of climate forecasts. This assumption, however, has been challenged, e.g., by Knutti et al. (2009) and Notz (2015) for coupled ocean-atmosphere models and, recently, by Löptien and Dietze (2017) and Löptien and Dietze (2019) for models of pelagic biogeochemical cycling.

A potential solution to this dilemma is the assessment of past climate states to test the sensitivity of climate models (as suggested by, e.g., Braconnot et al., 2012). The idea being that the geologic records of environmental responses to past climate changes complement the climate observations from the past decades such that respective fidelity metrics become indicative of the reliability of future projections.

In this regard, the isotopic composition ($\delta^{30}\text{Si}$) of biogenic silica (BSi) preserved in ocean sediments is of special interest to the field of pelagic biogeochemical ocean modeling. The reasons are: first, silicic acid (DSi) is an essential element for diatoms, which are autotrophic key players in the pelagic carbon cycle. Second, the isotopic composition of BSi is stable and preserves over millennia once secluded from processes at the water-sediment interface. Third, diatoms produce BSi with a $\delta^{30}\text{Si}$ distinctly different from the $\delta^{30}\text{Si}$ of their substrate DSi. The latter is caused by diatoms which tend to build more isotopically light BSi into their shells, compared to the $\delta^{30}\text{Si}$ in ambient DSi - a process also referred to as fractionation. This fractionation relates the $\delta^{30}\text{Si}$ of BSi in the sediments to the turnover of DSi by diatoms. The advantage of using the isotopic composition to improve our current understanding of glacial-interglacial cycles, instead of simply using BSi sediment burial rates, is that $\delta^{30}\text{Si}$ is less affected by water-column processes which are, on the one hand, unrelated to BSi production but may, on the other hand, modulate the amount of BSi that is preserved in the sediments.

69 A major challenge is the interpretation of $\delta^{30}\text{Si}$ of BSi records because the link be-
70 tween diatom DSi turnover and $\delta^{30}\text{Si}$ isotopic signature in BSi is complex (see also Rague-
71 neu et al., 2000). In a (Rayleigh) system, like a surface mixed layer in spring, diatoms
72 preferentially take up lighter DSi until only relatively heavy substrate is left (and sub-
73 sequently taken up). Hence, the $\delta^{30}\text{Si}$ isotopic signature in BSi is indicative of the amount
74 of substrate left, with high (low) values indicating oligotrophic (nutrient replete) con-
75 ditions. In contrast, in a system characterized by high incoming and outgoing physical
76 transports of substrate (e.g. a location within the Gulf Stream) the $\delta^{30}\text{Si}$ of BSi is pre-
77 dominantly determined by the $\delta^{30}\text{Si}$ of the constantly resupplied DSi - and only mod-
78 estly altered by the respective fractionation during BSi production because the fraction-
79 ation signal can not build up (since it is constantly flushed out of the local system). Both
80 the Rayleigh and the "flushed" system can be described to high precision by simple equa-
81 tions (e.g. Cloos et al., 2016, their equation 1 to 6). The difficulty is in the quantifi-
82 cation of the relation between physical transport flushing rate and biotic BSi export out
83 of the sun-lit surface ocean - or in other words: the relation between flushing and BSi
84 production needs to be known in order to interpret $\delta^{30}\text{Si}$ of BSi records. Further com-
85 plexity is potentially added by variations of the $\delta^{30}\text{Si}$ composition of DSi feeding the sur-
86 face waters.

87 In summary, both local (production and export of BSi, which is affected by local
88 environmental conditions) and remote processes (production and export upstream which
89 affects incoming environmental conditions), determine the isotopic signature of BSi at
90 a given location. This complex entanglement of ocean circulation and biogeochemistry
91 calls for the application of a 3-dimensional numerical model to guide the interpretation
92 of $\delta^{30}\text{Si}$ in observed BSi records. Indeed, the (modern climate) pioneering studies of Wis-
93 chmeyer et al. (2003) and Gao et al. (2016) illustrated the benefit of using a numerical
94 coupled ocean-circulation biogeochemical model in linking silicon isotopes to silicic acid
95 utilization.

96 Using models for interpretation in such ways leads, however, to a causality dilemma.
97 Coupled ocean-circulation biogeochemical models rely on a number of assumptions and
98 (often poorly known) model parameters (such as growth/death of phytoplankton and
99 sinking of organic matter to depth). Most of these assumptions and parameters are not
100 well constrained in the sense that different choices may result in an equally-good fit to
101 present day observations - but simultaneously very different projections (e.g. Löptien and
102 Dietze (2017), Löptien and Dietze (2019)). Thus, paleo records such as the isotopic com-
103 position of BSi preserved in ocean sediments, are of great interest to assess and reduce
104 such uncertainties. At the same time, these model uncertainties complicate the interpre-
105 tation of simulated past marine biogeochemical cycling in general (e.g., Hülse et al., 2017)
106 and of the isotopic composition of BSi preserved in ocean sediments in particular. An
107 aggravating circumstance is that the observational records are still so sparse (even for
108 present day $\delta^{30}\text{Si}$ DSi), such that Hendry and Brzezinski (2014) conclude that the data
109 set is "... inadequate to evaluate mechanisms leading to even the first-order distribution
110 of isotopes of Si in the global ocean".

111 Even so, a number of very interesting hypotheses, explaining aspects of spatial and
112 temporal variance in $\delta^{30}\text{Si}$ of BSi records, have been rooted on the available observational
113 records. Among them is the Silicic Acid Leakage Hypothesis which may explain glacial
114 interglacial atmospheric CO_2 changes (SALH, e.g., Brzezinski et al. (2002), Matsumoto
115 et al. (2002), Matsumoto et al. (2014)). In the following we outline the basic idea of the
116 SALH as far as the silicic acid is concerned (see, e.g. Matsumoto and Sarmiento, 2008,
117 as concerns its link to glacial interglacial atmospheric CO_2 changes): Today's South-
118 ern Ocean (SO) retains or traps DSi at the expense of more northward latitudes by a
119 combination of deep and efficient BSi export and meridional overturning. Driven by the
120 strong southern westerly wind belt, deep, nutrient replete waters are brought to the sur-
121 face at the Antarctic Divergence. The northward branch of the Divergence (which po-

122 tentially exports DSi from the SO) is efficiently stripped of DSi by phytoplankton. So,
 123 by the time the water reaches the Polar Front and the formation sites of Subantarctic
 124 Mode Waters (SAMW) and Antarctic Intermediate Waters (AAIW) which spread north-
 125 wards, most of the DSi has been exported as BSi to depth into the southward-flowing
 126 Circumpolar Deep Water (CDW). The CDW surfaces south of the Polar Front and, hence,
 127 the respective DSi is thereby retained in the SO. The SALH postulates that this DSi trap-
 128 ping in the SO was alleviated during glacial times triggered by e.g. enhanced iron sup-
 129 ply: the enhanced iron supply and associated physiological changes may have reduced
 130 the Si demands of diatoms, relative to the need of bioavailable nitrogen. Thus, left-over
 131 DSi might have leaked into the SAMW and AAIW and thereby could have left the SO.
 132 In summary, the SALH assumes that more DSi might have been available outside the
 133 SO during glacial times. A straightforward (Rayleigh) conclusion is that the glacial $\delta^{30}\text{Si}$
 134 was lower (as observed) because, according to the above considerations, DSi should have
 135 been less limiting relative to nitrogen.

136 The SALH and its relation to relatively low glacial $\delta^{30}\text{Si}$ (e.g., Sutton et al., 2018)
 137 has, however, been recently challenged by Frings et al. (2016) who concluded, based on
 138 a very comprehensive review, that consistent shifts among different ocean basins from
 139 low glacial $\delta^{30}\text{Si}$ to higher interglacial $\delta^{30}\text{Si}$ (0.5 – 1‰) may rather have been caused
 140 by a respective change in the isotopic composition of land-ocean fluxes of Si.

141 Our study adds to the ongoing discussion by exploring various hypotheses poten-
 142 tially triggering lower glacial $\delta^{30}\text{Si}$ in an Earth System Model of intermediate complex-
 143 ity. Our modeling approach builds on the pioneering works of Wischmeyer et al. (2003)
 144 and Gao et al. (2016) for modern climate and applies our extended model to both the
 145 Last Glacial Maximum and modern climate. Specifically, we explore the effects of (1)
 146 differences in the Si:N ratios, mimicking alleviated iron limitation during the LGM (Mat-
 147 sumoto et al., 2014), (2) differing winds during the LGM (e.g., Kohlfeld et al., 2012; McGee
 148 et al., 2010; Sime et al., 2013), (3) differing Si supply to the ocean during the LGM (Frings
 149 et al., 2016) and (4) a differing isotopic composition of Si supplied to the ocean during
 150 the LGM (Frings et al., 2016; Opfergelt et al., 2013). The underlying aim is to illustrate
 151 the complex entanglement of ocean circulation and biogeochemistry, which finally de-
 152 termines the isotopic composition of $\delta^{30}\text{Si}$ of BSi preserved in sediments.

153 2 Materials and Methods

154 2.1 Observations

155 We use the World Ocean Atlas 2009 data to assess our preindustrial (*PI*) simula-
 156 tion. More specifically, we compare against annual mean climatologies of temperature
 157 (Locarnini et al., 2010), salinity (Antonov et al., 2010), phosphate (Garcia et al., 2010)
 158 and silicate (Garcia et al., 2010).

159 Silicon isotopic data in seawater ($\delta^{30}\text{Si}$ of DSi) are put together from data published
 160 in Beucher et al. (2008,1); Cardinal et al. (2005); De La Rocha et al. (2011); de Souza
 161 et al. (2012a,1); Ehlert et al. (2012); Fripiat et al. (2011a,1,1); Grasse et al. (2013); Reynolds
 162 et al. (2006). A binning procedure increased horizontal data coverage: surface data with
 163 a nominal depth of 50 m refers to binning all data within 0-100 m. Abyssal data refers
 164 to binning all data within 1500-2500 m.

165 Silicon isotopic data in BSi as preserved in sediment cores is compiled, following
 166 Frings et al. (2016), from Brzezinski et al. (2002); De LaRocha et al. (1997); De La Rocha
 167 et al. (1998, 2011); Ehlert et al. (2013); Ellwood et al. (2010); Hendry et al. (2016,1); Horn
 168 et al. (2011); Pichevin et al. (2009).

169

2.2 Model

170

171

172

173

174

175

176

177

178

179

180

181

182

183

184

185

In this study we present numerical simulations with the University of Victoria Earth System Climate Model (UVic ESCM, Weaver et al., 2001). We present equilibrium simulations for two distinct climates, the preindustrial year 1800 (PI) and the Last Glacial Maximum (LGM) 21000 years before present and evaluate the model’s distribution of $\delta^{30}\text{Si}$ of BSi preserved in ocean sediments. UVic ESCM is an intermediate complexity model, featuring a simplified (vertically integrated) atmosphere. In contrast, the ocean dynamics is, although rather coarse, resolved in all three dimensions. The vertical resolution starts with 50 m at the surface of the ocean and gradually coarsens to 500 m in the abyss. The horizontal resolution of all model components (i.e., ocean, land, atmosphere, sea ice) is 1.8° in meridional and 3.6° in zonal direction. UVic’s assets are low computational demands and an extensive number of peer-reviewed studies including the description of LGM and PI equilibrium simulations. Among its drawbacks are a simplified atmosphere and a spatial resolution of the ocean that is coarse compared to, e.g., that class of models that underlie the current projections of the Intergovernmental Panel on Climate Change. Our simulations build on two configurations introduced by Brennan et al. (2012) already:

186

187

188

189

(1) *PI*, which refers to the "Preindustrial Equilibrium Simulation" described in Sec. 3 of Brennan et al. (2012). Briefly summarized, the atmospheric $p\text{CO}_2$ is set to 283.87 ppm and the orbital configurations to those representative of the year 1800. The initial conditions are those from the 5 kyr spinup from Brennan et al. (2012).

190

191

192

193

194

(2) *LGM*, which refers to the "Last Glacial Maximum Equilibrium Simulation" described in Sec. 4 of Brennan et al. (2012). Briefly summarized, the atmospheric $p\text{CO}_2$ is set to a low 189.65 ppm, the orbital parameters to those representing the conditions at 21 kyr BP and the surface elevation and albedo on land are adjusted following a reconstruction of Northern Hemisphere land ice (ICE-4G, Peltier (2009)).

195

196

197

198

199

200

The wind forcing during LGM consists of the same prescribed climatology (NCEP) used for the preindustrial simulations in our rather simple ESCM (see Weaver et al., 2001, for details). Rather weak dynamic wind feedbacks are parameterized as a function of surface temperature gradients and added to this climatology. The choice of building on a present day climatology is pragmatic, since the wind conditions during the LGM are discussed controversially (e.g. Kohlfeld et al., 2012; Sime et al., 2013).

201

2.2.1 Equations for the Si-Cycle

202

203

204

205

206

207

For this study we added an explicit and prognostic representation of (1) dissolved silicic acid (DSi), (2) biogenic Si (BSi), (3) that fraction of DSi that is composed of the silicon isotope ^{30}Si (D^{30}Si) and (4) that fraction of BSi that is composed of the silicon isotope ^{30}Si (B^{30}Si) to the original pelagic biogeochemical module used in Brennan et al. (2012). All prognostic biogeochemical variables C , at a given point in (model) space are determined following:

$$\frac{\partial C}{\partial t} = T + sms, \quad (1)$$

208

209

210

211

212

213

where T denotes the spatial divergence of diffusive and advective transports. sms refers to the source-minus-sinks term. The sms terms of the silicon module are adopted from Gao et al. (2016). The convenience of their approach is that the silicon module does not feed back onto the original biogeochemical model (of, in our case, Brennan et al. (2012)). Thus, our silicon isotope module is purely diagnostic in the sense that it does not alter the original climate and carbon cycles documented by Brennan et al. (2012) already.

214

215

216

The respective sms terms that describe the linkage of the silicic acid cycle with the pelagic biogeochemical cycle of Brennan et al. (2012) are described below. Approach and notation follow Gao et al. (2016). The DSi is supplied to the ocean at a temporally con-

217 stant rate, $RRDSi$ of $9.55 Tmol Si year^{-1}$ (Frings et al., 2016) and is homogeneously
 218 distributed over the surface ocean.

219 • **DSi equation:**

$$sms(DSi) = r BSi - P_{Si}, \quad (2)$$

220 where r denotes the diatom opal dissolution rate and P_{Si} denotes the biogenic opal
 221 production. r is temperature dependent:

$$r = A \exp(T/T_c), \quad (3)$$

222 with the parameters A setting the dissolution rate and T_c determining the tem-
 223 perature dependance of opal dissolution. The value of T_c is adopted from Gao et al.
 224 (2016) (see Table 1). The value of A has been determined in a tuning exercise (see
 225 Section 2.2.2), P_{Si} is calculated as a function of the production rate of particu-
 226 late organic matter $pomp$ (as calculated by the original biogeochemical module
 227 of Brennan et al., 2012) and DSi concentration:

$$P_{Si} = \min \left(pomp R_{Si:P} \frac{DSi}{K_{PHY}^{DSi} + DSi}, r_{Pro} DSi \right), \quad (4)$$

228 where, $R_{Si:P}$ denotes the molecular DSi to phosphate uptake ratio, associated with
 229 BSi production, K_{PHY}^{DSi} denotes the half-saturation constant of DSi uptake (see
 230 Table 1). r_{Pro} is the maximum rate of BSi production under non-limiting condi-
 231 tions.

232 • **BSi equation:**

$$sms(BSi) = -r BSi + P_{Si} - w \frac{\partial BSi}{\partial z}, \quad (5)$$

233 where, w is the sinking speed of BSi and $w \frac{\partial BSi}{\partial z}$ denotes the divergence of verti-
 234 cal BSi fluxes.

235 • **D³⁰Si equation:**

236 Following Gao et al. (2016) we include, in addition to total Si (i.e. the sum of the
 237 stable isotopes ²⁸Si, ²⁹Si, and ³⁰Si), an explicit representation of the silicon iso-
 238 tope ³⁰Si. During BSi production we apply the fractionation factor $\alpha_1 = 0.9989$
 239 (De LaRocha et al., 1997; Gao et al., 2016) which reduces the uptake of heavier
 240 ³⁰Si relative to the lighter Si stable isotopes.

$$sms(D^{30}Si) = r BSi \frac{B^{30}Si}{BSi} - P_{Si} \alpha_1 \frac{D^{30}Si}{DSi} \quad (6)$$

241 Following Gao et al. (2016), we assume no fractionation during BSi dissolution.

242 • **B³⁰Si equation:**

$$sms(B^{30}Si) = -r BSi \frac{B^{30}Si}{BSi} + P_{Si} \alpha_1 \frac{D^{30}Si}{DSi} - w \frac{\partial B^{30}Si}{\partial z}. \quad (7)$$

243 We calculate the silicon isotopic composition $\delta^{30}Si$ in units ‰ as a function of the
 244 total DSi (or BSi) concentration and D³⁰Si (or B³⁰Si) following:

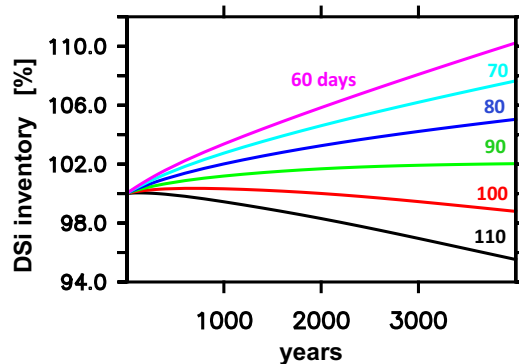
$$\delta^{30}Si = \left(\frac{(^{30}Si/^{28}Si)_{sample}}{(^{30}Si/^{28}Si)_{NBS-28}} - 1 \right) \cdot 10^3, \quad (8)$$

245 $(^{30}\text{Si}/^{28}\text{Si})_{NBS-28} = 0.0335$ (Coplen et al., 2002). We calculate ^{28}Si from the
 246 total Si and ^{30}Si concentrations as $^{28}\text{Si} = 0.953(\text{Si} - ^{30}\text{Si})$ which assumes that
 247 all stable isotopes other than the ^{28}Si and ^{30}Si always amount to 4.7% of total
 248 Si. (Here we follow Reynolds, 2009, stating that the assumption of a constant rel-
 249 ative abundance of the normalizing isotope "... is valid for small isotopic varia-
 250 tions described by the δ notation".)
 251 We set the isotopic composition $\delta^{30}\text{Si}$ of DSi supplied to the surface ocean (mim-
 252 icking e.g. river runoff) $\text{RR}\delta^{30}$ to 0.74 (Frings et al., 2016).

253 Our implementation of processes in the sediments is idealized. Once BSi sinks out of the
 254 lowermost wet model grid box it gets buried and leaves the system forever. A constant
 255 surface flux RRDSi (Table 1) replenishes what is lost by sedimentation - if the integra-
 256 tion is long enough so that the model can reach an equilibrium. Simulated $\delta^{30}\text{Si}$ of sed-
 257 imented BSi are taken as the simulated isotopic composition of BSi sinking out of the
 258 lowermost wet model grid box. This idealization is motivated by the urge to save com-
 259 putational resources that would otherwise be necessitated to equilibrate the sediment
 260 model.

261 2.2.2 Parameter Settings

262 The volume of the ocean is $1.4 \cdot 10^{18} \text{ m}^3$, containing an average DSi concentration
 263 of $92 \text{ mmol Si m}^{-3}$ (Garcia et al., 2010). This yields an oceanic inventory of $1.3 \cdot 10^{17} \text{ mol Si}$.
 264 Devision of the inventory with the supply rate of DSi (RRDSi , Table 1) to the ocean yields
 265 a timescale of 14 000 years. This timescale is a rough estimate of the residence time of
 266 DSi in the ocean consistent with the 9 000 to 16 000 year range estimated by Georg et al.
 267 (2009) and Tréguer et al. (1995), respectively. The residence time of DSi provides a lower
 268 bound on the time our model framework needs to adjust to changes to the formulation
 269 of Si cycling. It is also a measure of the expected equilibration timescale of the model.



270
 271 **Figure 1.** Temporal evolution of simulated preindustrial oceanic DSi inventory relative to ob-
 272 servations (WOA09 Garcia et al., 2010, also used to initiate the model) in units %. The different
 273 colors denote simulations with different opal dissolution rates (i.e. different choices of parameter
 274 A in Table 1). The colored numbers denote the respective inverse of parameter A in units days.
 275

271 The long equilibration timescale of our Si module calls for long wall-clock times until
 272 the effects of model changes can be evaluated reliably. This limits the number of model
 273 parameters (and formulations) that can be explored. Our approach here is to use the orig-
 274 inal model formulations and parameters from Gao et al. (2016) and to adjust only the
 275 opal dissolution rate A , such that the DSi inventory stays close to the observations from

Table 1. Reference model parameters of our implementation of the Gao et al. (2016) silicon module into the pelagic biogeochemical module of Brennan et al. (2012).

parameter	description	Gao et al. (2016)	our value	unit
A	opal dissolution rate	333^{-1}	90^{-1} (see Fig. 1)	day^{-1}
T_c	critical temperature of opal dissolution	12	12	$^{\circ}\text{C}$
$R_{Si:P}$	molecular DSi to phosphate stoichiometric ratio	25	25	$\frac{\text{mol DSi}}{\text{mol P}}$
K_{PHY}^{DSi}	half-saturation constant of DSi uptake during BSi production	4	4	$\frac{\text{mmol DSi}}{\text{m}^3}$
r_{Pro}	BSi production rate under non-limiting conditions	0.5	0.5	day^{-1}
w	sinking speed of BSi	10	10	$\frac{\text{m}}{\text{day}}$
RRDSi	total Si supply to the (surface) ocean (by e.g. river runoff)	9	9.55 (Frings et al., 2016)	$\frac{\text{Tmol Si}}{\text{year}}$
$\text{RR}\delta^{30}$	isotopic composition of (riverine) Si supply to the (surface) ocean	0.8	0.74 (Frings et al., 2016)	‰
α_1	^{30}Si fractionation factor during BSi production	0.9989	0.9989	[]
[]	fractionation factor during BSi dissolution	1	1	[]

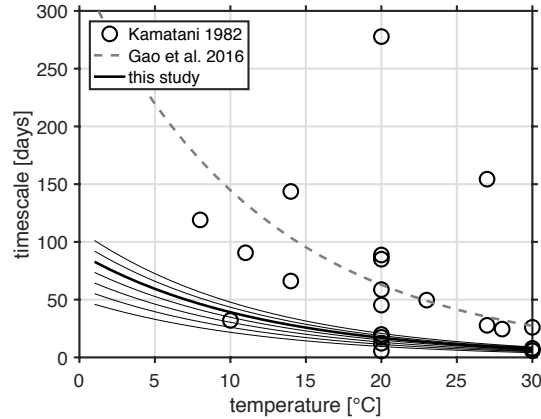


Figure 2. Inverse of dissolution rates of silica from diatoms as a function of ambient temperature. The circles denote data compiled by Kamatani (1982). Three values in excess of 300 days have been discarded here. The dashed grey line refers to settings in the model of Gao et al. (2016). The thick black line refers to the reference model setting in this study. The thin black lines refer to settings tested during tuning the DSi inventory.

276 Garcia et al. (2010). Fig. 1 shows that, to this end, the choice of $A = 90^{-1} \text{ days}^{-1}$
 277 is the best compromise between fast equilibration (which saved wall-clock time) and small
 278 misfit to observations (only two % overestimation of DSi inventory) among the choices
 279 of A tested in this study.

280 Fig. 2 shows the temperature dependance of silica dissolution rates that is asso-
 281 ciated with our choice of A : compared with Gao et al. (2016), our choice features sub-
 282 stantially faster dissolution rates, throughout the entire range of temperatures. When
 283 compared to data compiled by Kamatani (1982) it is, however, still consistent with ob-
 284 servations. On these grounds we justify our choice of $A = 90^{-1}$. We provide a respec-
 285 tive model assessment for the Si module in the Appendix A.

286 2.2.3 Experiments

287 As outlined above (Sect. 2.2), we run our reference model version under PI and LGM
 288 climate conditions to quasi-equilibrium (simulations *PI* and *LGM*). In a second step, start-
 289 ing from *LGM*, we perform a suite of sensitivity experiments for the LGM. Table B.1 lists
 290 these experiments, tailored to explore the sensitivity of our model towards environmen-
 291 tal changes. The focus is on changes that have been suggested in the literature to have
 292 engrained substantial signatures in the isotopic composition of $\delta^{30}\text{Si}$ of the BSi archived
 293 in oceanic sediments. These simulations are setup as follows:

- 294 • *LGMfe* is designed to mimic the effect of iron replete conditions on DSi uptake.
 295 As summarized by Matsumoto et al. (2014), there is evidence from incubation ex-
 296 periments that the Si:N consumption ratio is high under iron-depleted conditions
 297 (Franck et al., 2000; Hutchins and Bruland, 1998) and relatively low under iron
 298 replete conditions (Franck et al., 2000; Pondaven et al., 2000). In experiment *LGMfe*
 299 the molecular DSi to phosphate stoichiometric ratio $R_{\text{Si:P}}$ is reduced by 36%. Be-
 300 cause the N:P ratio is fixed to 16 in our model, this corresponds to a Si:N ratio
 301 of 1.
- 302 • *LGMbreezy* and *LGMslack* are designed to test the effect of potential glacial in-
 303 terglacial variability of climatological winds driving the ocean circulation: The wind

304 conditions during the LGM remain poorly constrained, such that even the sign
 305 of changes relative to today’s conditions is uncertain (e.g. Kohlfeld et al., 2012;
 306 McGee et al., 2010; Sime et al., 2013). In order to envelope the range of poten-
 307 tial effects on $\delta^{30}\text{Si}$ of BSi, we follow Matsumoto et al. (2014) and test both a global
 308 doubling of wind speeds and a halving, dubbed *LGMbreezy* and *LGMslack*, respec-
 309 tively. These changes affect only the momentum received by the ocean.

- 310 • *LGMflush* and *LGMtrickle* are designed to test the effect of potential glacial in-
 311 terglacial variability of riverine Si inputs into the ocean. Following Frings et al.
 312 (2016), who suggest, based on a literature review, that the river DSi flux has been
 313 within $\pm 20\%$ of today’s inputs during the LGM, we increase (decrease) the total
 314 supply of Si to the surface ocean by 20% in experiment *LGMflush* (*LGMtrickle*).
 315 Because reliable data regarding the variability of the spatial distribution of this
 316 input over time is sparse we distribute all input evenly over space.
- 317 • *LGMlight* is designed to test the idea of Frings et al. (2016) that the relatively low
 318 values of $\delta^{30}\text{Si}$ archived in glacial BSi are caused by an isotopically lighter com-
 319 position of riverine Si inputs to the ocean. Following Frings et al. (2016), *LGM-*
 320 *light* reduces the $\delta^{30}\text{Si}$ of DSi supplied to the ocean by 1‰. The underlying idea
 321 is that biotic and abiotic processes acting along the course of a river determine
 322 the isotopic composition of the runoff to the ocean. To this end, the study of Schoe-
 323 lynck et al. (2019) is a illustrative curiosity showing the effect of a single herd of
 324 hippos increasing $\delta^{30}\text{Si}$ by a sizable 0.2‰ in Mara River, Kenya. Further, there
 325 is evidence that the isotopic composition of groundwater inputs (Georg et al., 2009)
 326 and glacial meltwaters (Hawkins et al., 2018) may also have changed over glacial-
 327 interglacial cycles (Georg et al., 2009).

328 2.3 Manifestation Timescales

329 Our model investigations are all based on numerical time-slice experiments (i.e.,
 330 we run the model to quasi-equilibrium under the respective boundary conditions) - as
 331 opposed to investigating transient responses. Such an approach discards the informa-
 332 tion regarding the timescales on which model responses to disturbances manifest them-
 333 selves. This can spuriously illuminate links between processes and their manifestation
 334 in the isotopic composition of material archived in sediment cores. We thus measure ”man-
 335 ifestation timescales” by locally fitting exponential functions to the simulated $\delta^{30}\text{Si}$ -anomalies
 336 in BSi of the 10 000 year sensitivity experiments, listed in Table 2. Depending on the
 337 sign of changes in $\delta^{30}\text{Si}$ in BSi we fit either to:

$$f(t, x, y) = \alpha(x, y)e^{-\frac{t}{\tau(x, y)}}, \quad (9)$$

338 or

$$f(t, x, y) = \alpha(x, y) \left(1 - e^{-\frac{t}{\tau(x, y)}} \right), \quad (10)$$

339 where $f(t, x, y)$ is the accumulated change in $\delta^{30}\text{Si}$ of BSi at time t , longitude x and lat-
 340 itude y . The constant $\alpha(x, y)$ and the manifestation timescale $\tau(x, y)$ are estimated by
 341 using an unconstrained nonlinear minimization of the root mean square deviation be-
 342 tween the local exponential fit and simulated local changes in $\delta^{30}\text{Si}$ in BSi (Nelder–Mead,
 343 described in e.g. Lagarias et al., 1998, starting with an initial guess of $\tau = 100 \text{ years}$
 344 and $\alpha(x, y)$ as the difference of $\delta^{30}\text{Si}$ -anomalies between the start and the end of respec-
 345 tive time slice experiments).

346 3 Results

347 In the following subsections we explore the results of the sensitivity experiments
 348 regarding their ability to reproduce observed differences in the $\delta^{30}\text{Si}$ signature between

Table 2. Model simulations.

tag	description	initial conditions	duration of simulation
<i>PI</i>	"Preindustrial Equilibrium Simulation" of Brennan et al. (2012)	equilibrated simulation of Brennan et al. (2012)	10000 yr
<i>LGM</i>	"Last Glacial Maximum Equilibrium Simulation" of Brennan et al. (2012)	equilibrated simulation of Brennan et al. (2012)	20000 yr
<i>LGMfe</i>	identical to <i>LGM</i> except for Si:N stoichiometric ratio reduced to 1, mimicking the effect of iron replete conditions	end of LGM	10000 yr
<i>LGMbreezy</i>	identical to <i>LGM</i> except for a doubling in all winds, driving the oceanic circulation	end of LGM	10000 yr
<i>LGMslack</i>	identical to <i>LGM</i> except for a halving of all winds, driving the oceanic circulation	end of LGM	10000 yr
<i>LGMflush</i>	identical to <i>LGM</i> except for 20% increase in land-ocean DSi supply	end of LGM	10000 yr
<i>LGMtrickle</i>	identical to <i>LGM</i> except for 20% decrease in land-ocean DSi supply	end of LGM	10000 yr
<i>LGMlight</i>	identical to <i>LGM</i> except for a 1‰ decrease in $\delta^{30}\text{Si}$ of land-ocean DSi supply	end of LGM	10000 yr

349 LGM and PI. Each of the sensitivity experiments builds on a scenario of environmental
 350 LGM conditions proposed earlier in the literature (see Section 2.2.3; Table B.1). The
 351 major aim is to dissect mechanisms that lead to reasonable agreement with the obser-
 352 vations and paleoarchive data.

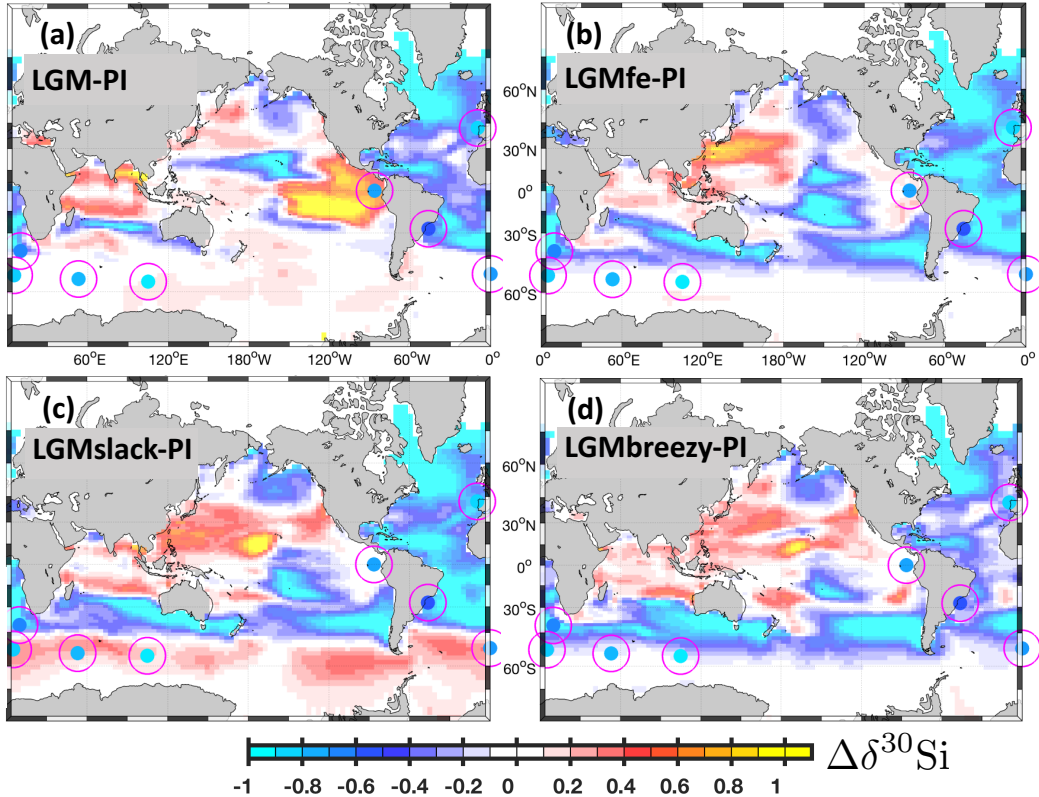


Figure 3. Difference in simulated $\delta^{30}\text{Si}$ of BSi relative to the preindustrial simulation *PI* as deposited to sediments in units ‰. Panel (a), (b), (c) and (d) refer to differences *LGM-PI*, *LGMfe-PI*, *LGMslack-PI* and *LGMbreezy-PI*, respectively. Magenta circles denote locations of observations of $\delta^{30}\text{Si}$ in BSi as preserved in sediment cores (see Section 2.1).

3.1 LGM

353

354 Figure 3 panel (a) shows the difference between the LGM "reference" simulation
 355 *LGM* and our preindustrial simulation *PI*. We find that the colder glacial climate, over-
 356 all, increases $\delta^{30}\text{Si}$ of BSi deposited to the sediments (relative to *PI*). This is inconsis-
 357 tent with observations typically featuring lower glacial $\delta^{30}\text{Si}$. (An exception to this rule
 358 is the Atlantic Ocean where simulated glacial $\delta^{30}\text{Si}$ of BSi are lower and roughly con-
 359 sistent with observations.)

360 In order to set a reference point for the following discussions (in this Section) we
 361 dissect the processes that imprint the wrong sensitivity into simulation *LGM*: key to un-
 362 derstanding is that *LGM* features an oceanic DSi inventory that is 15% lower relative
 363 to that in *PI*. This is puzzling because the export of BSi across 120 m depth (which con-
 364 stitutes the origin of all BSi sinking to depth) is also reduced by a substantial 30% dur-
 365 ing the colder LGM climate. Given that the riverine supply of Si is identical in *LGM* and
 366 *PI*, this is counterintuitive. Further investigations revealed that the process behind this

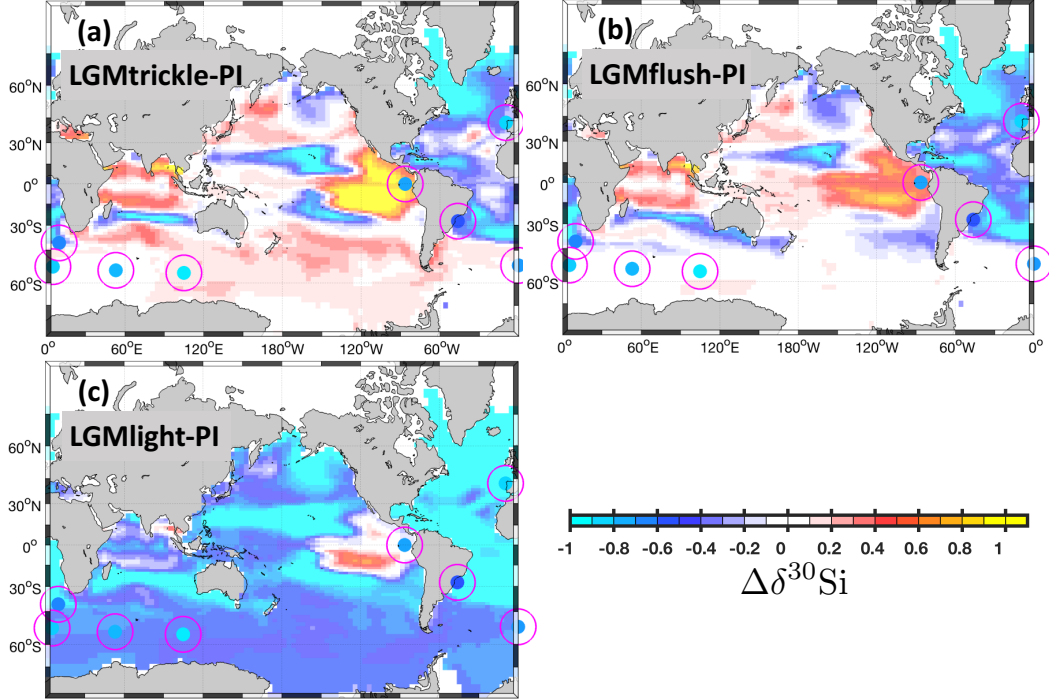


Figure 4. Difference in simulated $\delta^{30}\text{Si}$ of BSi relative to the preindustrial simulation *PI* as deposited to sediments in units ‰. Panel (a), (b) and (c) refer to differences *LGMtrickle-PI*, *LGMflush-PI* and *LGMlight*, respectively. Magenta circles denote locations of observations of $\delta^{30}\text{Si}$ in BSi as preserved in sediment cores (see Section 2.1).

367 conundrum is the antagonistic effect of temperature on BSi sedimentation rate in our
 368 model framework. *LGM* features, consistent with observational evidence (e.g., Margo Project
 369 Members, 2009), an average of 2°C colder oceanic temperature than *PI*. In combination
 370 with an increase in sea-ice cover during the *LGM*, which shields the ocean from photo-
 371 synthetically active radiation essential for autotrophic growth, this slows down the global
 372 primary production and associated export of organic material from the sun-lit surface
 373 to depth. Hence, less BSi is produced and less BSi is set on its way sinking to the sed-
 374 iments. This reduction in BSi production is, however, overcompensated by a reminer-
 375 alization rate that is also slowed down by the lower temperatures such that more organic
 376 material reaches the seafloor before it is remineralized and dissolved. A rough scaling,
 377 assuming steady state (and horizontal uniformity which reduces the problem to one spa-
 378 tial dimension), puts the potential of this effect into perspective: the vertical flux of sink-
 379 ing BSi described in Equation 5 is, following the notation of Kriest and Oeschles (2008),
 380 given by

$$F(z') = F_0 \exp\left(-\frac{rz'}{\bar{w}}\right), \quad (11)$$

381 where $F(z')$ is the sinking flux at depth z' defined as that distance between actual depth
 382 and the depth of the euphotic zone. F_0 is the flux out of the euphotic zone. The sink-
 383 ing speed \bar{w} is 10 m day^{-1} (see Table 1), and r as defined by our Equation 3. For an ocean
 384 with a uniform temperature of 4°C Equation 11 (such as in *PI*) yields a sedimentation
 385 efficiency (here defined as the ratio between flux to the sediment and export out of the
 386 euphotic zone) of 2‰. A reduction of temperature down to 2°C (such as in *LGM*) yields
 387 5‰. Hence, a reduction of only 2°C yields a substantial (initial) 2.5-fold increase in re-
 388 spective sedimentation rates. It is this temperature-driven increase in sedimentation ef-

389 efficiency that reduces the global availability of DSi and, consequently, increases overall
390 $\delta^{30}\text{Si}$ in our *LGM* simulation relative to *PI*.

391 As concerns the decreasing $\delta^{30}\text{Si}$ of BSi in the Atlantic Ocean, which outweighs the
392 globally-reversed trend, we find: north of 55°N the simulated DSi inventory is substan-
393 tially higher during the LGM, relative to *PI* (Figure A.3). This is owed to fundamen-
394 tally different global circulation patterns in *PI* and *LGM*. In *PI* the upper branch of the
395 meridional overturning circulation (MOC) supplies the North Atlantic with surface wa-
396 ters that are already relatively depleted in DSi because of biologically induced BSi ex-
397 port from the surface to depth. The lower branch of the MOC exports deep waters en-
398 riched in BSi such that the DSi content of the Atlantic Ocean is relatively low. Simu-
399 lation *LGM* differs in that sea ice protrudes down to 52°N (in winter) which shields res-
400 pective algae from essential photosynthetically active radiation. This reduced vertical
401 export of BSi meets throttled meridional overturning circulation (2 Sv versus 18 Sv in
402 the simulation *PI*) which puts an end to the cycle that reduces the DSi inventory of the
403 Atlantic Ocean. The supply of DSi to the surface ocean is identical in *PI* and *LGM*. It
404 has a prescribed, relatively (compared to surface values in the North Atlantic) low $\delta^{30}\text{Si}$
405 value of 0.74‰ and is evenly distributed over the ocean in our model (see Section 2.2.1).
406 This eventually reduces the $\delta^{30}\text{Si}$ of BSi in the glacial Atlantic Ocean because it is no
407 longer (or far less) counteracted by the peculiar interplay between biology and MOC de-
408 scribed above.

409 3.2 LGMfe

410 The simulation *LGMfe* anticipates that more bioavailable iron was available dur-
411 ing the LGM. We mimic this effect by reducing the DSi demands by 36% relative to the
412 nitrogen (and phosphorous) demands in our model. This decelerates the biogeochem-
413 ical cycling of DSi which - according to the Silicic Acid Leakage Hypothesis (SALH) -
414 would reduce the DSi trapping efficiency of the SO. The basic idea behind today's rel-
415 atively efficient DSi trapping in the SO is that surface waters on their way north out of
416 the SO get depleted of nutrients (DSi) by biologic (BSi) export to depth into southward
417 moving water masses, thereby "trapping" DSi in the SO. By decelerating the cycling of
418 DSi (e.g. by reducing the Si quota in sinking organic matter), the major trapping mech-
419 anism is weakened and the hypothesis is that this results in net DSi export, or leakage,
420 out of the SO.

421 We define a measure of leakage or respective reduction in the "DSi trapping effi-
422 ciency" as the ratio between oceanic inventory south of 40°S and the total global DSi
423 inventory. Comparing *LGMfe* with *LGM* we find a reduction of only one percent. This
424 rather minute change is outweighed by the effect of the the 36% reduction in DSi demands,
425 described above, which leads to a substantially damped biogeochemical DSi cycling and
426 a reduction of BSi export to the sediments. The latter results in a global increase in the
427 oceanic DSi content of 11%. Hence, even though the trapping efficiency in the SO is re-
428 duced, the SO does not lose DSi but rather gains $\approx 10\%$ relative to simulation *LGM*.
429 The increase in both local (in the SO) and global DSi concentrations triggers an over-
430 all decrease in $\delta^{30}\text{Si}$ of BSi (Fig. 3 panel (b)) which is generally roughly consistent with
431 observations as far as the sign of changes in concerned. An exception being the SO, where
432 simulated changes are too weak, and at some locations even of opposite sign when com-
433 pared to the observations.

434 3.3 LGMslack and LGMbreezy

435 The simulations *LGMslack* and *LGMbreezy* assume, in contrast to the reference sim-
436 ulation, that glacial winds differed from those today. Sign and magnitude of the change
437 is controversially discussed in the literature. Here we test both, a global halving *LGM-*
438 *slack* and a doubling *LGMbreezy* of wind speeds. The results are depicted in Fig. 3, pan-

439 els (c) and (d), with *LGMslack* featuring a generally higher $\delta^{30}\text{Si}$ of BSi in the SO, sug-
 440 gesting a straightforward underlying process: reduced winds bring less DSi up to the sun-
 441 lit surface which increases the effect of fractionating DSi uptake by algae in surface DSi
 442 (because there is less "flushing" of the system). As the substrate (surface DSi) becomes
 443 higher in $\delta^{30}\text{Si}$, so does the associated BSi export.

444 In contrast, in *LGMbreezy* more DSi is upwelled in the SO. The effect of fractiona-
 445 tion on the isotopic composition of the substrate is diluted by the additional DSi sup-
 446 ply. As a consequence $\delta^{30}\text{Si}$ of BSi mostly decreases and is consistent with observations
 447 in terms of the sign of simulated changes. But specifically in the SO *LGMbreezy* features
 448 a sensitivity which is apparently too low.

449 Complexity is added to the rest of the ocean as the system adjusts: enhanced (de-
 450 creased) upwelling of nutrients by winds feed an increase (decrease) in export produc-
 451 tion which results in a global Si loss (gain) by increased (decreased) sedimentation such
 452 that the initial nutrient pulse is counteracted. Negative values, both in *LGMslack* and
 453 *LGMbreezy* follow the overall patterns already discussed for *LGM*.

454 In summary, our model suggests that reduced winds are inconsistent with observed
 455 $\delta^{30}\text{Si}$ of BSi in the SO. In contrast, the effect of increasing winds appear to be more con-
 456 sistent with the observations of $\delta^{30}\text{Si}$ of BSi as far as the sign of changes is considered.
 457 In terms of magnitude, however, a doubling of the wind during the LGM fails to retrace
 458 most of the observations in the SO.

459 3.4 LGMtrickle and LGMflush

460 The experiments *LGMtrickle* and *LGMflush* assume that the supply of Si to the
 461 glacial ocean was different from today's. The default value (applied in all of our config-
 462 urations except the two discussed here) for total supply of Si to the ocean (RRDSi) is
 463 $9.55 \text{ Tmol Si year}^{-1}$ with an isotopic composition corresponding to 0.74‰ (RR δ^{30} ; Ta-
 464 ble 1). The fractionating effect of marine biota increases the global mean $\delta^{30}\text{Si}$ of DSi
 465 relative to the supply because it preferentially exports BSi with lower $\delta^{30}\text{Si}$ to the sed-
 466 iment such that DSi with higher $\delta^{30}\text{Si}$ remains in the water column. From this we con-
 467 clude that the larger (smaller) the supply in relation to the biotic turnover the lower (higher)
 468 the $\delta^{30}\text{Si}$ in DSi - which ultimately controls the isotopic composition of BSi archived in
 469 sediments.

470 Fig. 4 supports this conclusion: panel (a) shows the difference between the simu-
 471 lation *LGMtrickle* and *PI*. Compared to panel (a) in Fig. 3, we find that the 20% reduc-
 472 tion of Si supply to the ocean drives an overall increase in $\delta^{30}\text{Si}$ of BSi. Likewise, panel
 473 (b) in Fig. 4 shows that a 20% increase in Si supply decreases the overall $\delta^{30}\text{Si}$ of BSi
 474 with the biggest effect concentrated in the eastern equatorial upwelling area.

475 In summary, the sensitivity of $\delta^{30}\text{Si}$ of BSi to changes in Si supply is too small to
 476 explain observed glacial interglacial variations. Expressed in terms of a global average
 477 of $\delta^{30}\text{Si}$ of BSi, we find less than 0.1‰ change when altering the Si supply by 40% in Si.

478 3.5 LGMlight

479 Frings et al. (2016) suggest that the relatively low $\delta^{30}\text{Si}$ of BSi archived in glacial
 480 sediments are caused by a glacial isotopic composition of the Si supplied to the ocean
 481 that was 1‰ lighter than today. Consistent with their reasoning, we find in Fig. 4 panel
 482 (c) a global decrease in $\delta^{30}\text{Si}$ of BSi by up to 1‰ (with the eastern tropical Pacific be-
 483 ing an exception) in response to the reduction of RR δ^{30} . Expressed in terms of a global
 484 oceanic average we find a decrease of 0.65‰ at the end of our 10 000 year spinup.

485 In summary, Fig. 4 panel (c) suggests that a reduction of $\delta^{30}\text{Si}$ in DSi supplied to
 486 the ocean drives changes that are consistent with almost all observations of glacial $\delta^{30}\text{Si}$
 487 in BSi archived in sediments.

488 4 Discussion

489 In Section 4.1 we discuss timescales at work, Section 4.2 puts the results into per-
 490 spective and Section 4.3 discusses potential and generic sources of uncertainties in the
 491 underlying Earth System Model.

492 4.1 Manifestation Timescales

493 So far we explored the sensitivity of our model to changes in environmental con-
 494 ditions with numerical time-slice experiments. This can be deceptive for, e.g., processes
 495 that manifest themselves with timescales as long or longer than typical glacial interglacial
 496 cycles. In the following we use the concept of manifestation timescale introduced in Sec-
 497 tion 2.3. in order to check if our simulated isotopic signatures of processes could possi-
 498 bly be detected in actual sediments - as opposed to being smeared out over one or more
 499 glacial interglacial cycles.

500 Fig. 5 shows that manifestation timescales vary considerably over space. In terms
 501 of detectability, we find in *LGMLight* that manifestation timescales at the observational
 502 sites are short enough so that they should be detectable in sediments (if they were to
 503 have been at play). This suggests that the effect of changing isotopic composition of oceanic
 504 Si supply to the ocean would be clearly imprinted into the sediment record. This does
 505 not apply to *LGMBreezy* where manifestation timescales in the Southern Ocean exceed
 5000 years (not shown).

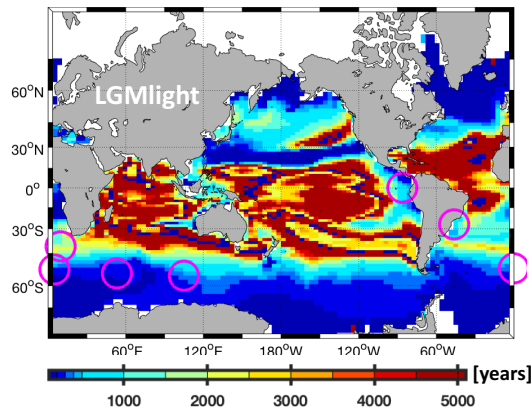


Figure 5. Timescale of manifestation of changes in $\delta^{30}\text{Si}$ of BSi archived in sediments simulated in *LGMLight* (as shown in Figure 3 panel c) in units years. White patches denote changes of less than 0.1‰ or regions with bottom BSi concentrations less than $10^{-10} \text{ mol Si m}^{-3}$. Magenta circles denote locations of observations of $\delta^{30}\text{Si}$ in BSi as preserved in sediment cores (see Section 2.1).

506

507 4.2 Appraisal of Results

508 The two experiments *LGMBreezy* and *LGMLight*, out of our total of 7 numerical sensi-
 509 tivity experiments, feature the best fit with respect to the sign to the overall, lower (rel-

510 ative to today) glacial $\delta^{30}\text{Si}$ of BSi observations. This holds especially in the Southern
 511 Ocean. The experiment with increased winds (*LGMbreezy*), however, features a sensi-
 512 tivity which, although of correct sign, is much lower than suggested by observational ev-
 513 idence. In addition *LGMbreezy* features very long manifestation timescales (when com-
 514 pared to *LGMlight*; cf., Sect. 4.1) which implies that the process of increasing winds is,
 515 in reality, even harder to detect than the rather weak signal we find at the end of our
 516 10 000 year long numerical time slice experiment suggests. This leaves us with simula-
 517 tion *LGMlight* being the most consistent with observations of $\delta^{30}\text{Si}$ of BSi out of all con-
 518 sidered processes (listed, e.g., in Table B.1).

519 Even so, other processes such as changes to air-sea iron fluxes and wind fields may
 520 also have been at play. According to our model results, however, these should manifest
 521 themselves more prominently in metrics other than in the isotopic composition of BSi.
 522 One example of such a metric are sedimentary redox-sensitive trace-metal records. Jac-
 523 card et al. (2016) deduce from respective evidence glacially reduced dissolved oxygen con-
 524 centrations in the Atlantic Sector of the deep SO. Figure 6 suggests that, in our model,
 525 a decrease in wind speeds does drive a consistent oxygen decrease while unchanged winds,
 526 or an increase of winds, result in an inconsistent increase of simulated dissolved oxygen
 527 concentrations. Investigations of the link between decreasing winds and oxygen reveals
 528 two antagonistic processes being at work in our model. For one, the reduced wind-induced
 529 upwelling of nutrients drives less production and associated oxygen consumption in the
 530 SO. This, on its own, would increase the oxygen concentration. However, this process
 531 is opposed by a reduced wind-induced overturning which reduces ventilation and drives
 532 an oxygen decrease. The net effect differs among the sectors of the SO, such that the At-
 533 lantic Sector in Figure 6 panel (b) is consistent with results from Jaccard et al. (2016).
 534 The difference among the Sectors in the SO is facilitated by a reduced (down to 40% rel-
 535 ative to *LGM*) Antarctic Circumpolar Current which reduces the zonal mixing between
 536 the Sectors as a result of reduced winds supplying less momentum to the ocean. Please
 537 note that a comprehensive analysis of oceanic deoxygenation, which must cover the role
 538 of (preferably explicitly resolved) iron dynamics (see, e.g. Stoll, 2020) and more data (e.g.
 539 Jaccard and Galbraith, 2011), is beyond the scope of this manuscript which focuses on
 540 the isotopic composition of BSi in response to changing environmental conditions. Our
 541 main conclusion here is that *LGMbreezy* is apparently inconsistent with sedimentary redox-
 542 sensitive trace-metal records.

543 4.3 Model Uncertainties

544 Assessing the reliability of model projections is not straight-forward. This applies
 545 to both, climate models (Notz, 2015) and pelagic biogeochemical models (Löptien and
 546 Dietze, 2017). Our approach here is to highlight a choice of our simplifying *ad-hoc* as-
 547 sumptions which may potentially degrade our model results:

- 548 • DSi supply by rivers. In our simulations, all DSi supplied from the land into the
 549 ocean is homogeneously distributed over the oceans. The rationale behind this is
 550 the sparse information available on glacial-interglacial changes in river loads and
 551 the implicit assumption that horizontal transports act on much shorter timescales
 552 than the vertical transports. Among the (unintended) consequences is a glacial
 553 Arctic Ocean which is continuously flushed by isotopically light DSi in our model
 554 - even though - in reality, it was covered by ice and probably did not receive any
 555 river runoff at all.
- 556 • Isotopic fractionation during BSi dissolution. In our setup this is not to account
 557 for - an approach we share with the pioneering 3-dimensional modeling work of
 558 Wischmeyer et al. (2003), the box modeling work of Reynolds (2009), and the 3-
 559 dimensional modeling work of Gao et al. (2016). Our simulation of deep $\delta^{30}\text{Si}$ of
 560 DSi (see, Figure A.7) fits into this successive model development in that it fea-
 561 tures a realistic gradient in the deep waters of the Atlantic and Pacific Oceans.

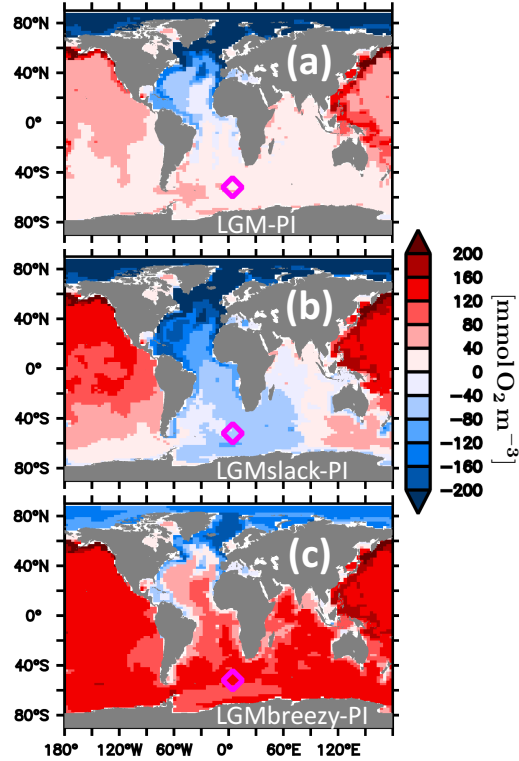


Figure 6. Simulated oxygen concentration at the bottom of the ocean relative to simulated preindustrial (PI) concentrations in units $\text{mmol O}_2 \text{ m}^{-3}$. Panel (a), (b) and (c) refer to simulations *LGM*, *LGMslack* and *LGMbreezy*, respectively.

562 In comparison, the early work of Wischmeyer et al. (2003) failed to simulate a sig-
 563 nificant gradient (less than 0.1‰ difference), while Reynolds (2009) and Gao et al.
 564 (2016) reported a more realistic difference of 0.3‰ between the basins. Our model
 565 features 0.5‰ which is even closer to the data-constrained model estimate of 0.7‰
 566 by Holzer and Brzezinski (2015) - arguably the most comprehensive estimate of
 567 today's $\delta^{30}\text{Si}$ of DSi distribution in the deep ocean. Further comparison with the
 568 Holzer and Brzezinski (2015) estimate, however, reveals that our simulated vari-
 569 ance in the deep Pacific is apparently too low: while results by Holzer and Brzezinski
 570 (2015) suggest a range between 1.7‰ in the South and 1.1‰ up North, we find
 571 barely any variation in our simulation *PI*. According to Holzer and Brzezinski (2015)
 572 and Beucher et al. (2008) this deficiency of our model is linked to not accounting
 573 for isotopic fractionation during BSi dissolution.

- 574 • Diagenetic DSi release from sediments. The results presented here are based on
 575 a setup which neglects DSi release from sediments - even though it is known to
 576 be a significant agent in the world ocean silica cycle (Tréguer and De La Rocha,
 577 2013). This simplification was necessitated by the computational burden that is
 578 associated with the long timescales of sedimentary processes. In order to test for
 579 robustness of our results, however, we followed up a suggestions that surfaced dur-
 580 ing the review process. As described in more detail in Appendix B we decreased
 581 the export of BSi out of the lowermost wet model grid box in order to mimic the
 582 effects of diagenetic DSi release from the sediments. In summary: the thereby mod-
 583 ified model version which is more complex in the sense that it contains more tun-
 584 able model parameters performed better in terms of simulated DSi concentrations.
 585 As concerns the misfit between simulated glacial interglacial $\delta^{30}\text{Si}$ of BSi differ-

586 ences we find that our results as shown in Figure 3 a are robust (when compared
587 with Figure B.2).

- 588 • Variable Si isotopic fractionation by diatoms. We apply the constant fractiona-
589 tion factor $\alpha_1 = 0.9989$ (De LaRocha et al., 1997; Gao et al., 2016) even though
590 contradictory evidence suggests that fractionation factors vary among species (Sut-
591 ton et al., 2013) and that Fe availability may modulate fractionation (Cavagna et al.,
592 2011; Meyerink et al., 2017).

593 A problematic region where our model simulations deviate substantially from ob-
594 servations of $\delta^{30}\text{Si}$ of BSi is the eastern equatorial Pacific in Fig. 3 and 4. We speculate
595 that this is associated with an unrealistic zonal circulation in our model which is appar-
596 ently endemic to the current generation of coupled ocean circulation biogeochemical mod-
597 els (Dietze and Loptien, 2013; Getzlaff and Dietze, 2013).

598 In summary, we refer to a model that is capable of reproducing the effects of (prein-
599 dustrial) circulation and isotopic fractionation during BSi production with a fidelity com-
600 parable to existing non data-assimilated 3-dimensional coupled ocean circulation biogeo-
601 chemical models. Compared with the arguably most comprehensive data-assimilated model
602 estimate of the present abyssal δ^{30} of DSi we miss an intra-basin variability in the Pa-
603 cific Ocean that is probably linked to unaccounted isotopic fractionation during BSi dis-
604 solution.

605 5 Conclusions

606 We set out to simulate $\delta^{30}\text{Si}$ of BSi (such as opal) archived in oceanic sediments
607 under modern climates (PI) and glacial conditions (LGM). Specifically, we implement
608 and test several hypothesis which were suggested in the literature to explain the observed
609 difference in $\delta^{30}\text{Si}$ of BSi between PI and LGM.

610 Our numerical experiments with an Earth System Model of intermediate complex-
611 ity suggest that neither of the following processes effected glacial-interglacial changes in
612 the isotopic composition of BSi is consistent with observations: (1) an overall cooling and
613 substantial reduction of the meridional overturning circulation (our experiment *LGM*),
614 (2) a decrease of Si:N quota in diatoms as potentially effected by increased air-sea iron
615 fluxes (our experiment *LGMfe*), (3) decreasing winds (our experiment *LGMslack*) and
616 (4) increasing or decreasing Si supply to the ocean (our experiments *LGMtrickle* and *LGM-*
617 *flush*).

618 Out of seven sensitivity experiments, only the simulation with increased winds (ex-
619 periment *LGMbreezy*) and the simulation with a changed isotopic composition of river
620 runoff (experiment *LGMlight*) reproduce the observed sign of change, specifically in the
621 SO. The experiment with increasing winds (experiment *LGMbreezy*), however, fails to
622 reproduce the magnitude of observed changes and is, furthermore, inconsistent with the
623 Jaccard et al. (2016) estimate of dissolved near-bottom oxygen concentrations (based on
624 redox-sensitive trace-metal records archived in the sediments in the Atlantic Sector of
625 the SO). The experiment *LGMlight* is most consistent with observed changes in $\delta^{30}\text{Si}$ of
626 BSi in terms of both, sign and magnitude. This confirms the suggestions by Frings et al.
627 (2016) that changes in the isotopic composition of DSi supplied to the ocean (rather than
628 changes in the internal oceanic cycling of DSi) triggered low glacial $\delta^{30}\text{Si}$ of BSi. Fur-
629 ther, the estimated manifestation timescale of changes in $\delta^{30}\text{Si}$ of BSi range between sev-
630 eral hundreds to 2500 years at the observational sites. This means that the respective
631 signal should be detectable - despite a global turnover timescale of DSi, which is com-
632 parable to the period of glacial-interglacial cycles.

633 As a side aspect we find a simulated oceanic DSi inventory which is 10-20% lower
634 during the Last Glacial Maximum than today. This is somewhat counterintuitive because

635 simulated BSi production is also lower during the LGM which suggests that less BSi
 636 is sinking down to the oceanic sediment. More comprehensive analysis shows that this ef-
 637 fect is outweighed by BSi dissolution rates that are also slowed down as a consequence
 638 of colder temperatures such that more BSi escapes dissolution prior to sedimentation in
 639 our model.

640 Caveats remain. A major problem of developing a Si module within the framework
 641 of an Earth System Model is the high computational cost associated with running test
 642 simulations to equilibrium. To this end, a turnover timescale of Si in the ocean of more
 643 than 10 000 years is a real handicap. Among the simplifications we chose in order to limit
 644 the number of test simulations was discarding the effect of fractionation during BSi dis-
 645 solution. According to Holzer and Brzezinski (2015) and Beucher et al. (2008) this may
 646 be the reason why our model does not reproduce observed variations of $\delta^{30}\text{Si}$ of DSi within
 647 the Pacific. Further - substantial - uncertainty is added by the generic problem of con-
 648 straining global biogeochemical ocean models (Löptien and Dietze (2015); Löptien and
 649 Dietze (2017); Löptien and Dietze (2019)).

650 A Model Assessment

651 The UVic ESCM reference version we use for *LGM* and *PI* has been described and
 652 assessed by Brennan et al. (2012). We left this base module unchanged. In the follow-
 653 ing we refer to our extension adding an Si-cycle (which does not feedback onto the origi-
 654 nal modules) in the following.

655 Figure A.1 shows the modern climate (PI) simulated DSi concentrations at the sur-
 656 face and at depth compared to observations (Garcia et al., 2010). A comparison of panel
 657 (a) and (c) suggests that the simulated DSi concentrations are somewhat too high at the
 658 surface, specifically in the tropics and the southern part of the Southern Ocean. At the
 659 same time, DSi concentrations are too low at the bottom, specifically in the northern Pa-
 660 cific (panel (b) and (d)). These deviations are also visible in the global mean profiles in
 661 Fig. A.2.

Table A.1. Comparison between observations (OBS) and preindustrial simulation (*PI*). Temp.,
 Sal., std., RMS, corr. coeff. and var refer to temperature, salinity, standard deviation, root mean
 square error between *PI* and OBS, and variance, respectively. $\delta^{30}\text{DSi}$ refers to surface values.
 The origin of observations is documented in Section 2.1.

variable	unit	std. OBS	std. <i>PI</i>	bias (<i>PI</i> -OBS)	RMS	corr. coeff.	var(<i>PI</i> ref)/ var(OBS)
Temp.	$^{\circ}\text{C}$	6.5	6.6	0.6	1.4	0.98	103%
Sal.	<i>PSU</i>	0.6	0.5	0.03	0.3	0.85	70%
PO_4	mmol P m^{-3}	0.83	0.77	-0.03	0.3	0.94	86%
O_2	$\text{mmol O}_2 \text{ m}^{-3}$	77	75	2	28	0.93	95%
DSi	mmol Si m^{-3}	54	40	11	30	0.84	54%
$\delta^{30}\text{DSi}$	‰	0.62	0.48	0.57	0.56	0.51	60%

662 We suspect that these differences are both the result of our choice of parameters
 663 (possibly an underestimated opal sinking velocity and an underestimated molecular DSi
 664 to phosphate stoichiometric ratio or an underestimated BSi production rate) as well as
 665 being caused by rather coarse spatial resolution of the ocean module which is known to
 666 retard ocean transports (e.g. Getzlaff and Dietze, 2013). An additional cause for model

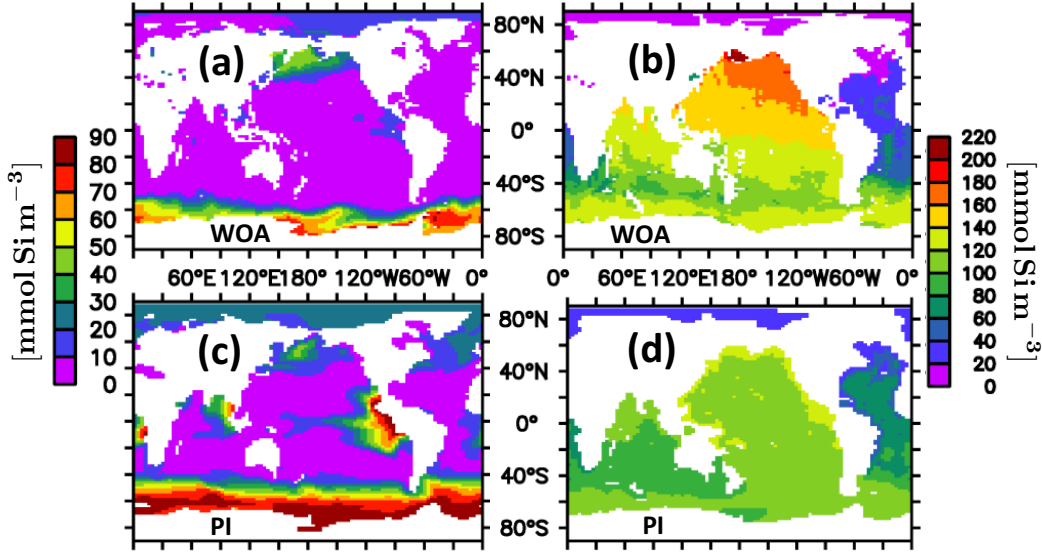


Figure A.1. Surface and deep (2000 m to bottom average) DSi concentrations in units $mmol Si/m^3$. (a) and (b) refer to surface and abyssal observations (Garcia et al., 2010), respectively. (c) and (d) refer to simulated preindustrial (PI) surface and abyssal concentrations, respectively.

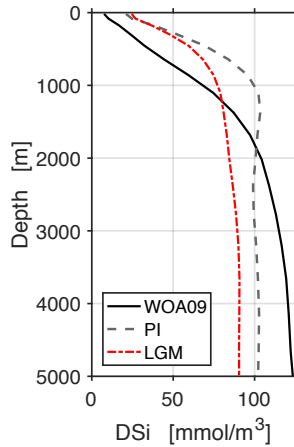


Figure A.2. Zonally and meridionally averaged vertical profile of DSi concentrations in units $mmol Si/m^3$. The black, grey dashed, and red dot-dashed lines refer to observations (black line, Garcia et al., 2010), preindustrial simulation, and Last Glacial Maximum simulation, respectively.

667 data misfits of DSi concentrations is followed up in the Appendix B where we added a
 668 brief investigation into the effect of diagenetic DSi release from sediments.

669 Figure A.3 depicts the zonally averaged export of DSi. While the above mentioned
 670 biases map also onto this metric, the major features are, nevertheless, captured. Specif-
 671 ically the trapping of DSi in the SO, high values in the tropics and a large drop in the
 672 Arctic are clearly visible. Not well captured are, however, the mid latitudes in the north-
 673 ern hemisphere where the simulated export is underestimated. Further, the transition

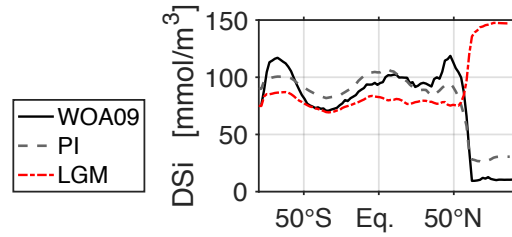


Figure A.3. Zonally and vertically averaged DSi concentrations in units $mmol Si m^{-3}$. The black, grey dashed, and red dot-dashed lines refer to observations (black line, Garcia et al., 2010), preindustrial simulation, and Last Glacial Maximum simulation, respectively.

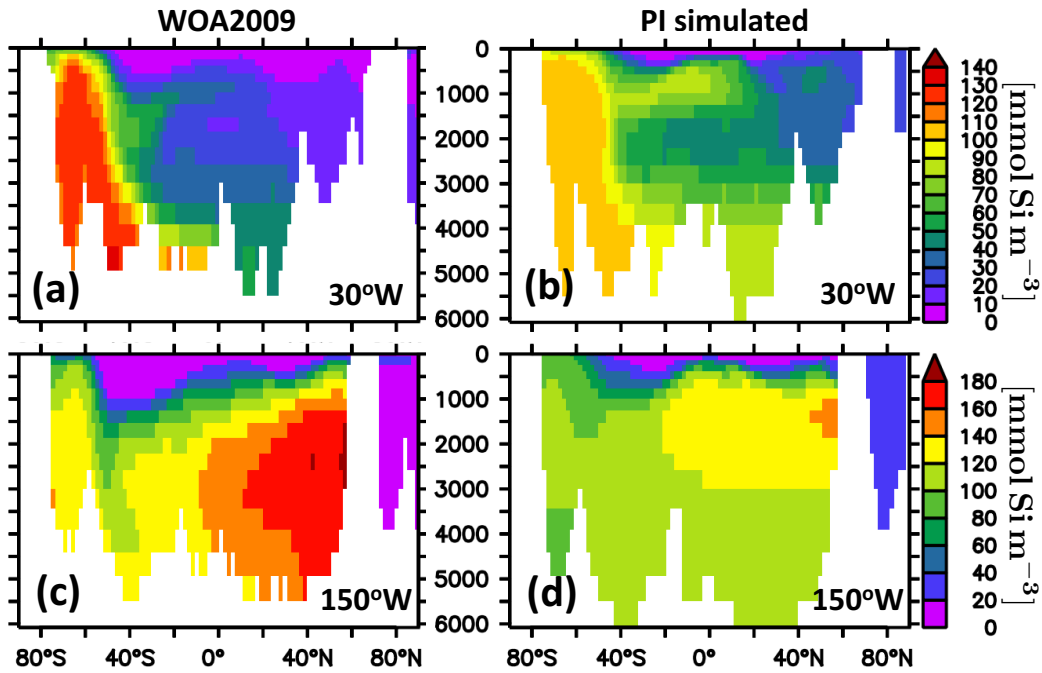


Figure A.4. Meridional sections over depth (in m) of DSi in units $mmol Si m^{-3}$. Panel (a) and (c) refer to observations (Garcia et al., 2010) and panel (b) and (d) to the preindustrial simulation.

674 zone to the SO is not as sharp as observed and DSi values in the Arctic are somewhat
 675 overestimated.

676 The Figures A.4 and A.5 show meridional sections of both, simulated DSi and
 677 phosphate in comparison to the observations. This allows for a continuative exploration
 678 of the reasons for model-data mismatches with respect to DSi : the section through the
 679 Atlantic (at 30°W) shows simulated DSi concentrations that are generally underestimated
 680 while phosphate seems in better agreement with the observations in that respect. In the
 681 SO, however, both variables are biased - and the biases oppose one another: in terms
 682 of SO nutrient trapping, simulated phosphate is trapped more efficiently than indicated
 683 by the observations. This is mirrored by the low bias of simulated SO dissolved oxygen
 684 concentrations (Figure A.6) indicating an overestimation of accumulated remineraliza-
 685 tion. This is in contrast to simulated DSi concentrations, where the simulated SO nu-
 686 trient trapping is too weak. With one nutrient biased high and the other nutrient biased

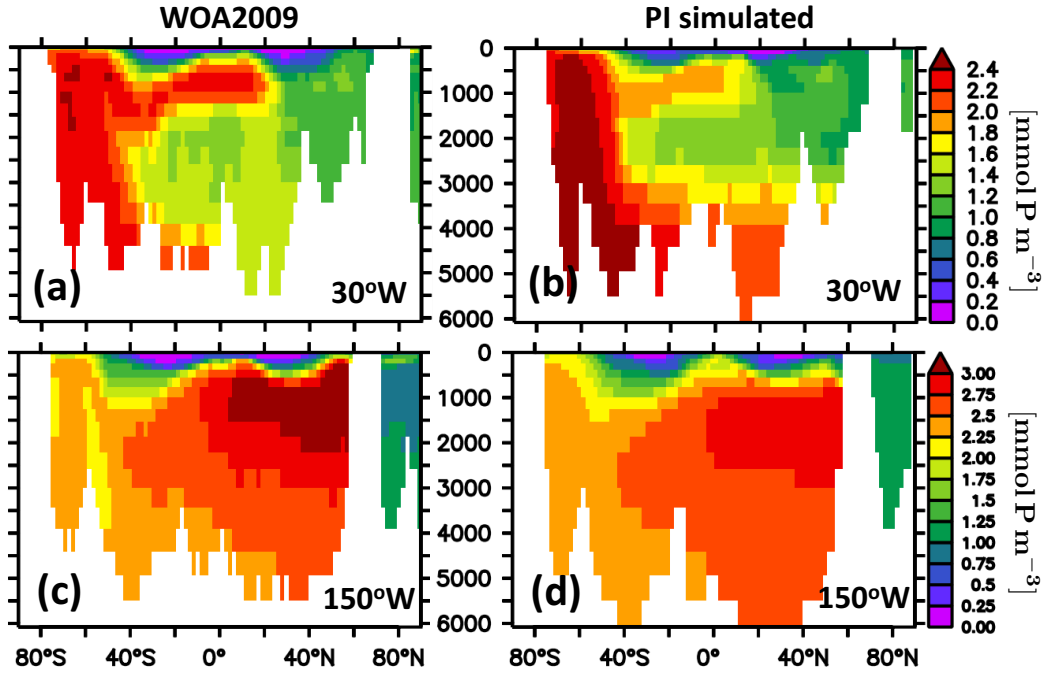


Figure A.5. Meridional sections over depth (in m) of PO₄ in units $mmol P m^{-3}$. Panel (a) and (c) refer to observations (Garcia et al., 2010) and panel (b) and (d) to the preindustrial simulation.

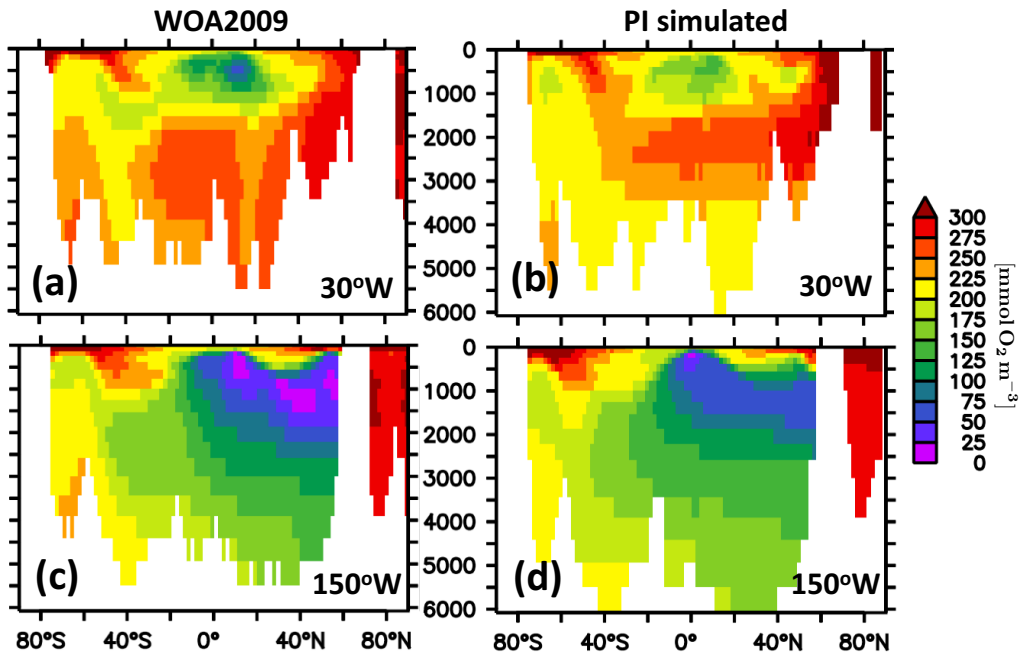


Figure A.6. Meridional sections over depth (in m) of dissolved O₂ in units $mmol O_2 m^{-3}$. Panel (a) and (c) refer to observations (Garcia et al., 2010) and panel (b) and (d) to the preindustrial simulation.

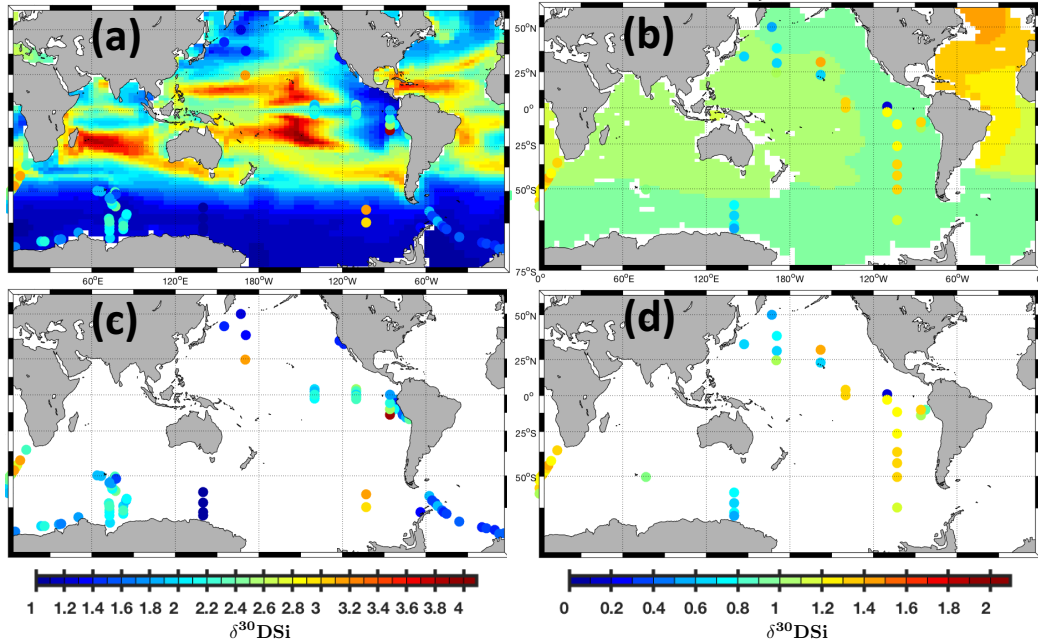


Figure A.7. $\delta^{30}DSi$ at the surface (50 m, panel (a) & (c)) and at depth (2000 m, panel (b) & (d)) in units ‰. The colored blobs denote those observations (see Section 2.1) within 0-100 m (1500-2500 m) that are closest to the nominal depth of 50 m (2000 m). The background color in panel (a) and (b) refers to simulation PI. Panel (c) and (d) show respective observations only to facilitate their recognition.

687 low it seems unlikely that a deficient circulation is the cause for these biases (although
 688 this can not be ruled out). Hence, the SO nutrient trapping apparently relates strongly
 689 to the biogeochemical model parameters. One conclusion from this may be that the bio-
 690 geochemical model is better tuned with respect to phosphate than to DSi. This is to be
 691 expected because of the wider use of the phosphate-based biogeochemical model and the
 692 much shorter equilibration time scales for phosphate which facilitate the respective tun-
 693 ing to observations. In the Pacific, however, the situation differs, and subsurface max-
 694 ima in the northern hemisphere (except the Arctic) are too low for both phosphate and
 695 DSi. Following our reasoning above this may be indicative for flaws in the ocean circula-
 696 tion module. Please note, however, that the attribution of flaws in model behavior to
 697 respective processes is challenging and may even be impossible given the current set of
 698 observations (e.g. Löptien and Dietze, 2019).

699 Table A.1 provides a quantitative estimate of how our DSi/BSi module compares
 700 against the underlying biogeochemical and ocean circulation module of Brennan et al.
 701 (2012). The simulated temperature variance is overestimated by 3% and the tempera-
 702 ture bias is 0.6 K, corresponding to 9% relative to the standard deviation in the obser-
 703 vations. The respective bias to standard deviation of salinity is with 0.03 even smaller
 704 (5% relative to the standard deviation in the observations). Simulated phosphate con-
 705 centrations are, surprisingly, even closer to observations than simulated salinities (note
 706 that this does also apply to simulated dissolved oxygen concentrations): the bias to stan-
 707 dard deviation ratio is smaller (4%) and the simulated variance covers 86% of observed
 708 levels (versus 70% for salinity). Given that the salinity distribution directly affects ocean
 709 circulation via density driven pressure gradients, it is remarkable that the misfit in this
 710 active physical property can be much larger than the misfit of the rather passive (in terms

of their effect on circulation) phosphate whose distribution is directly shaped by oceanic circulation. This may be an indication that the biogeochemical module of Brennan et al. (2012) has been "overly successfully" tuned to a flawed physics (a process illustrated by Löptien and Dietze, 2019). In contrast, the simulated DSi features the largest deviations among the metrics reviewed here. The simulation features a variance corresponding to 54% of observed levels and the simulated bias is 21% relative to the observed standard deviation. The correlation of simulated DSi concentrations with observations is, however, rather good in the sense that it is very similar to that of salinity (0.84 versus 0.85).

Fig. A.7 shows our simulated preindustrial $\delta^{30}\text{DSi}$ distribution. The sparseness of observational data with often times puzzling inhomogeneities illustrates the Hendry and Brzezinski (2014) conclusion that the $\delta^{30}\text{DSi}$ data set is "... inadequate to evaluate mechanisms leading to even the first-order distribution of isotopes of Si in the global ocean". Also we are urged to compare point observations to large scale averages, resolved by the model. The relatively low correlation of 0.51 between model and observations has thus to be considered with some caution. Please note that a clearer picture seems to be found for the more abrupt events of the deglacial, leading to the Silic Acid Ventilation Hypothesis of Hendry and Brzezinski (2014).

B Silica dissolution rates, temperature and diagenetic DSi release from sediments

One of the major processes at work in our simulations is a reduced glacial oceanic DSi inventory (relative to preindustrial). Lower glacial temperatures slow down BSi dissolution such that more BSi sinks into the sediments where it is lost forever in our model. In turn, the overall reduced availability of DSi invokes more DSi limitation which manifests itself in a glacial tendency towards higher $\delta^{30}\text{DSi}$ which is apparently inconsistent with the observed tendency to generally lower glacial $\delta^{30}\text{DSi}$.

During the review process of an earlier version of this manuscript the following concerns were put forward: our model does not account for diagenetic release of DSi from sediments even though it is known to be substantial (e.g., Tréguer and De La Rocha, 2013). Hence, our model neglects a process that retains Si in the ocean. Even so, our simulated DSi inventory is close to observations - because we adjusted the silica dissolution rate accordingly (Figure 1). This procedure yielded a functional dependency of silica dissolution and temperature which is at the lower end of data compiled by Kamatani (1982) and shown in Figure 2. In the following we will discuss if this may have flawed our results.

We integrate an additional set of model simulations dubbed PI^* and LGM^* for 10000 years (starting from the spunup simulations PI and LGM). PI^* and LGM^* are identical to PI and LGM except for: (1) We use the Gao et al. (2016) opal dissolution rate $A = 333^{-1} \text{day}^{-1}$ which yields a functional dependency of silica dissolution and temperature which is at the upper end of data compiled by Kamatani (1982) and shown in Figure 2. (2) We reduce the sinking velocity of BSi out of the lowermost wet model grid box from 10m day^{-1} down to 0.5m day^{-1} in order to mimic the effect of diagenetic DSi release (or, more specifically, the increased residence time of Si at the bottom of the water column).

Integration of PI^* for 10000 years resulted in a fairly equilibrated DSi inventory close to observations ($\approx 3\%$ less than Garcia et al., 2010). The DSi concentrations of PI^* are more realistic than in the reference version PI . In terms of route mean square error the misfit drops substantially from 30 (Table A.1) down to 15mmol Si m^{-3} (Table B.1). The increase in realism is confirmed by visually inspecting Figure B.2 versus Figure A.4.

760 In terms of $\delta^{30}DSi$ we find that PI^* features a variance more similar to observa-
 761 tions compared to PI (93% versus 60%; Table B.1 versus Table A.1). The correlation does,
 762 however, not improve probably because we do not account for isotopic fractionation dur-
 763 ing BSi dissolution (see discussion in Section 4.3).

764 In summary, PI^* features a more realistic DSi distribution, more realistic levels of
 765 $\delta^{30}DSi$ variance and a (rough) representation of diagenetic DSi release from the sedi-
 766 ments. Further, PI^* features a functional dependency of silica dissolution and temper-
 767 ature that is the upper end of data compiled by Kamatani (1982) - as opposed to PI which
 768 features a functional dependency that is at the lower end. Even so the glacial-interglacial
 769 sensitivity of $\delta^{30}Si$ of BSi is apparently robust: Figure B.2 shows the LGM^* - PI^* dif-
 770 ference that is similar to the respective LGM - PI difference in Figure 3 in that the sim-
 771 ulated changes are opposing the observational evidence.

Table B.1. Comparison between observations (OBS) and preindustrial simulation (PI^*). std., RMS, corr. coeff., var refer to standard deviation, root mean square error between simulation PI^* and OBS, and variance, respectively. $\delta^{30}DSi$ refers to surface values. The origin of observations is documented in Section 2.1.

variable	unit	std. OBS	std. PI	bias (PI -OBS)	RMS	corr. coeff.	var($PIref$)/var(OBS)
DSi	$mmol Si m^{-3}$	54	49	-1.2	15	0.96	83%
$\delta^{30}DSi$	‰	0.62	0.60	-0.29	0.58	0.54	93%

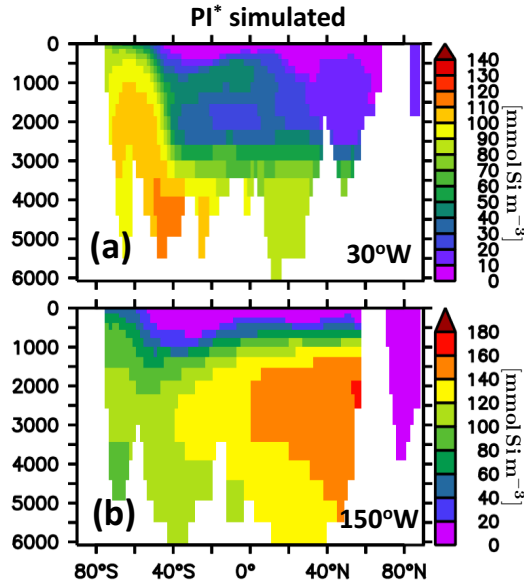


Figure B.1. Meridional sections over depth (in m) of DSi in units $mmol Si m^{-3}$. Panel (a) and (b) refer to simulation PI^* that applies the Gao et al. (2016) opal dissolution rate $A = 333^{-1} day^{-1}$ and that mimics diagenetic release of DSi from sediments by reducing the sinking velocity of BSi from $10 m day^{-1}$ to $0.5 m day^{-1}$ in the lowermost wet model grid box.

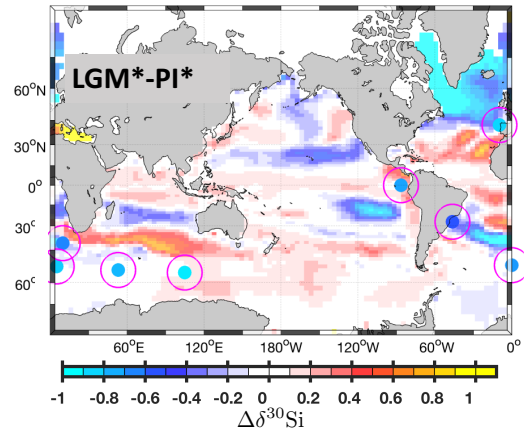


Figure B.2. Difference in simulated LGM $\delta^{30}\text{Si}$ of BSi relative to the preindustrial simulation PI^* as deposited to sediments in units ‰. The difference to Figure 3 (a) is that both LGM^* and PI^* refer to simulations that apply the Gao et al. (2016) opal dissolution rate $A = 333^{-1}\text{day}^{-1}$ and that mimic diagenetic release of DSi from sediments by reducing the sinking velocity of BSi from 10 m day^{-1} to 0.5 m day^{-1} in the lowermost wet model grid box.

772 Acknowledgments

773 H. D. and U. L. acknowledge funding by Deutsche Forschungsgemeinschaft (DFG) in the
 774 framework of the priority program *Antarctic Research with comparative investigations*
 775 *in Arctic ice areas SPP 1158* by grant no. *SCHN 762/5-1*. We acknowledge discussions
 776 with Mark Holzer and Katrin Meissner. Katrin Meissner provided the model configu-
 777 ration by sharing code and forcing files. Fruitful discussion with Richard Matear and An-
 778 drew Lenton were made possible by DFG grant no. *DI 1665/6-1* and *LO 1377/5-1*. A
 779 number of very good review papers eased the entry of H. D. and U. L. into the field. We
 780 are grateful to each and everyone sharing observational data. Data is available through
 781 Locarnini et al. 2010, Antonov et al. 2010, Garcia et al. 2010, Beucher et al. 2008, Car-
 782 dinal et al. 2005, De La Rocha et al. 2011, de Souza et al. 2012, Ehlert et al. 2012, Fripi-
 783 at et al. 2011, Grasse et al. 2013, Reynolds et al. 2006, Frings et al. 2016, Brzezinski
 784 et al. 2002, De La Rocha et al. 1997, De La Rocha et al. 1998, De La Rocha et al. 2011,
 785 Ehlert et al. 2013, Ellwood et al. 2010, Hendry et al. 2012, Hendry et al. 2016, Horn
 786 et al. 2011, and Pichevin et al. 2009. We thank one anonymous reviewer, Christoph Voelker
 787 and the editorial team for their constructive work and effort!

References

- 788
- 789 Antonov, J. I., Seidov, D., Boyer, T. P., Locarnini, R. A., Mishonov, A. V., Garcia,
790 H. E., Baranova, O. K., Zweng, M. M., and Johnson, D. R., (2010). World
791 Ocean Atlas 2009, Volume 2: Salinity. S. Levitus, Ed. NOAA Atlas NESDIS
792 69, U.S. Government Printing Office, Washington, D.C., 184pp.
- 793 Basile-Doelsch, I., (2006). Si stable isotopes in the Earth's surface: A review. *Journal*
794 *of Geochemical Exploration*, 88, 252–256, doi:10.1016/j.gexplo.2005.08.050.
- 795 Bauer, P., Thorpe, A., and Brunet, G., (2015). The quiet revolution of numerical
796 weather prediction. *Nature*, 525, 7567, 47–55, doi:10.1038/nature14956.
- 797 Beucher, C. P., Brzezinski, M. A., and Jones, J. L., (2008). Sources and biological
798 fractionation of Silicon isotopes in the Eastern Equatorial Pacific. *Geochimica*
799 *et Cosmochimica Acta*, 72, 3063–3073, doi:10.1016/j.gca.2008.04.021.
- 800 Beucher, C. P., Brzezinski, M. A., and Jones, J. L., (2011). Mechanisms controlling
801 silicon isotope distribution in the Eastern Equatorial Pacific. *Geochimica et*
802 *Cosmochimica Acta*, 75, 4286–4294, doi:10.1016/j.gca.2011.05.024.
- 803 Braconnot, P., Harrison, S. P., Kageyama, M., Bartlein, P. J., Masson-Delmotte,
804 V., Abe-Ouchi, A., Otto-Bliesner, B., and Zhao, Y., (2012). Evaluation of cli-
805 mate models using palaeoclimatic data. *Nature Climate Change*, 2, 417–424,
806 doi:10.1038/NCLIMATE1456.
- 807 Brennan, C. E., Weaver, A. J., Eby, M., and Meissner, K. J., (2012). Modelling Oxy-
808 gen Isotopes in the University of Victoria Earth System Climate Model for
809 Preindustrial and Last Glacial Maximum Conditions. *Atmosphere-Ocean*, 50,
810 4, 447–465, doi:10.1080/07055900.2012.707611.
- 811 Brzezinski, M. A., Pride, C. J., Franck, V. M., Sigman, D. M., Sarmiento, J. L.,
812 Matsumoto, K., Gruber, N., Rau, G. H., and Coale, K. H., (2002). A switch
813 from Si(OH)₄ to NO₃⁻ depletion in the glacial Southern Ocean. *Geophysical*
814 *Research Letters*, 29, 12, 1564, doi:10.1029/2001GL014349.
- 815 Cardinal, D., Alleman, L. Y., Dehairs, F., Savoye, N., Trull, T. W., and André, L.,
816 (2005). Relevance of silicon isotopes to Si-nutrient utilization and Si-source
817 assessment in Antarctic waters. *Global Biogeochemical Cycles*, 19, GB2007,
818 doi:10.1029/2004GB002364.
- 819 Cavagna, A.-J., Fripiat, F., Dehairs, F., Wolf-Gladrow, D., Cisewski, B., Savoye,
820 N., André, L., and Cardinal, D., (2011). Silicon uptake and supply during a
821 Southern Ocean iron fertilization experiment (EIFEX) tracked by Si isotopes.
822 *Limnology and Oceanography*, 56, 1, 147–160, doi:10.4319/lo.2011.56.1.0147.
- 823 Closset, I., Cardinal, D., Rembauville, M., Thil, F., and Blain, S., (2016). Un-
824 veiling the Si cycle using isotopes in an iron-fertilized zone of the Southern
825 Ocean: from mixed-layer supply to export. *Biogeosciences*, 13, 6049–6066,
826 doi:10.5194/bg-13-6049-2016.
- 827 Coplen, T. B., Hopple, J. A., Böhlke, J. K., Peiser, H. S., Rieder, S. E., Krouse,
828 H. R., Rosman, K. J. R., Ding, T., Vocke, Jr., R. D., Révész, K. M., Lamberty,
829 A., Taylor, P., and De Bièvre, (2002). *Compilation of Minimum and Maximum*
830 *Isotope Ratios of Selected Elements in Naturally Occurring Terrestrial Materi-*
831 *als and Reagents*, Water-Resources Investigation Report, 01-4222, 1–110, U.S.
832 Department of the Interior and U.S. Geological Survey, Reston Virginia.
- 833 De La Rocha, C. L., Brzezinski, M. A., and De Niro, M. J., (1998). Fractiona-
834 tion of silicon isotopes by marine diatoms during biogenic silica formation.
835 *Geochimica et Cosmochimica Acta*, 61, 23, 5051–5056, doi:10.1016/S0016-
836 7037(97)00300-1.
- 837 De La Rocha, C. L., Brzezinski, M. A., De Niro, M. J., and Shemesh, A., (1998).
838 Silicon-isotope composition of diatoms as an indicator of past oceanic change.
839 *Nature*, 395, 680–683, doi:10.1038/27174.
- 840 De La Rocha, C. L., Bescont, P., Croguennoc, A., Ponzevera, E., (2011). The sili-
841 con isotopic composition of surface waters in the Atlantic and Indian sectors
842 of the Southern Ocean. *Geochimica et Cosmochimica Acta*, 75, 5283–5295,

- 843 doi:10.1016/j.gca.2011.06.028.
- 844 de Souza, G. F., Reynolds, B. C., Johnson, G. C., Bullister, J. L., and Bourdon, B.,
845 (2012a). Silicon stable isotope distribution traces Southern Ocean export of Si
846 to the South Pacific thermocline. *Biogeosciences*, 9, 4199–4213, doi:10.5194/bg-
847 9-4199-2012.
- 848 de Souza, G. F., Reynolds, B. C., Rickli, J., Frank, M., Saito, M. A., Gerringa,
849 L. J. A., and Bourdon, B., (2012). Southern Ocean control of silicon stable
850 isotope distribution in the deep Atlantic Ocean. *Global Biogeochemical Cycles*,
851 26, GB2035, doi:10.1029/2011GB004141.
- 852 Dietze, H., and Löptien, U., (2013). Revisiting "nutrient trapping" in global coupled
853 biogeochemical ocean circulation models. *Global Biogeochemical Cycles*, 27,
854 265–284, doi:10.1002/gbc.20029.
- 855 Ehlert C., Grasse, P., Mollier-Vogel, E., Bösch, T., Franz, J., de Souza, G. F.,
856 Reynolds, B. C., Stramma, L., and Frank, M., (2012). Factors controlling
857 the silicon isotope distribution in waters and surface sediments of the Pe-
858 ruvian coastal upwelling. *Geochimica et Cosmochimica Acta* 99, 128–145,
859 doi:10.1016/j.gca.2012.09.038.
- 860 Ehlert, C., Grasse, P., and Frank, M., (2013). Changes in silicate utilisation and
861 upwelling intensity off Peru since the Last Glacial Maximum - insights from
862 silicon and neodymium isotopes. *Quaternary Science Reviews*, 72, 18–35,
863 doi:10.1016/j.quascirev.2013.04.013.
- 864 Ellwood, M. J., Wille, M., and Maher, W., (2010). Glacial Silicic Acid Con-
865 centration in the Southern Ocean. *Science*, 330, 6007, 1088–1091,
866 doi:10.1126/science.1194614.
- 867 Franck, V. M., Brzezinski, M. A., Coale, K. H., and Nelson, D. M., (2000). Iron
868 and silicic acid concentrations regulate Si uptake north and south of the Polar
869 Frontal Zone in the Pacific Sector of the Southern Ocean. *Deep-Sea Research*
870 *Part II*, 47, 3315–3338, doi:10.1016/S0967-0645(00)00070-9.
- 871 Frings, P. J., Clymans, W., Fontorbe, G., De La Roche, C. L., and Conley, D. J.,
872 (2016). The continental Si cycle and its impact on the ocean Si isotope budget.
873 *Chemical Geology*, 425, 12–36, doi:10.1016/j.chemgeo.2016.01.020.
- 874 Fripiat, F., Cavagna, A.-J., Dehairs, F., Speich, S., André, L., and Cardinal, D.,
875 (2011). Silicon pool dynamics and biogenic silica export in the Southern Ocean
876 inferred from Si-isotopes. *Ocean Science*, 7, 533–547, doi:10.5194/os-7-533-
877 2011.
- 878 Fripiat, F., Cavagnam A.-J., Savoye, N., Dehairs, F., André, L., and Cardinal, D.,
879 (2011). Isotopic constraints on the Si-biogeochemical cycle of the Antarc-
880 tic Zone in the Kerguelen area (KEOPS). *Marine Chemistry*, 123, 11–22,
881 doi:10.1016/j.marchem.2010.08.005.
- 882 Fripiat, F., Cavagna, A.-J., Dehairs, F., de Brauwere, A., André, L., and Cardinal,
883 D., (2012). Processes controlling the Si-isotopic composition in the Southern
884 Ocean and application for paleoceanography. *Biogeosciences*, 9, 2443–2457,
885 doi:10.5194/bg-9-2443-2012.
- 886 Gao, S., Wolf-Gladrow, D. A., and Völker, C., (2016). Simulating the modern $\delta^{30}\text{Si}$
887 distribution in the oceans and in marine sediments. *Global Biogeochemical*
888 *Cycles*, 30, 120–133, doi:10.1002/2015GB005189.
- 889 Garcia, H. E., Locarnini, R. A., Boyer, T. P., and Antonov, J. I., Baranova, O. K.,
890 Zweng, M. M., and Johnson, D. R., (2010). *World Ocean Atlas 2009, Volume*
891 *3: Dissolved Oxygen, Apparent Oxygen Utilization, and Oxygen Saturation*.
892 S. Levitus, Ed. NOAA Atlas NESDIS 70, U.S. Government Printing Office,
893 Washington, D.C., 344 pp.
- 894 Garcia, H. E., Locarnini, R. A., Boyer, T. P., and Antonov, J. I., (2010). *World*
895 *Ocean Atlas 2009, Volume 4: Nutrients (phosphate, nitrate, silicate)*. S. Levi-
896 tus, Ed. NOAA Atlas NESDIS 71, U.S. Government Printing Office, Washing-
897 ton, D.C., 398 pp.

- 898 Grasse, P., Ehlert, C., and Frank, M., (2013). The influence of water mass mixing on
899 the dissolved Si isotope composition in the Eastern Equatorial Pacific. *Earth*
900 *and Planetary Science Letters*, 380, 60–71, doi:10.1016/j.epsl.2013.07.033.
- 901 Getzlaff, J., and Dietze, H., (2013). Effects of increased isopycnal diffusivity mimick-
902 ing the unresolved equatorial intermediate current system in an earth system
903 climate model. *Geophysical Research Letters*, 40, 10, doi:10.1002/grl.50419.
- 904 Georg, R. B., West, A. J., Basu, A. R., and Halliday, A. N., (2009). Silicon fluxes
905 and isotope composition of direct groundwater discharge into the Bay of
906 Bengal and the effect on the global ocean silicon isotope budget. *Earth and*
907 *Planetary Science Letters*, 283, 67–74, doi:10.1016/j.epsl.2009.03.041.
- 908 Hawkins, J. R., Hatton, J. E., Hendry, K. R., de Souza, G. F., Wadham, J. L.,
909 Ivanovic, R., Kohler, T. J., Stibal, M., Beaton, A., Lamarche-Gagnon, G., Ted-
910 stone, A., Hain, M. P., Bagshaw, E., Pike, J., and Tranter, M., (2018). The
911 silicon cycle impacted by past ice sheets. *Nature Communicationa*, 9, 3210,
912 doi:10.1038/s41467-018-05689-1.
- 913 Hendry, K. R., and Brzezinski, M. A., (2014). Using silicon isotopes to un-
914 derstand the role of the Southern Ocean in modern and ancient bio-
915 geochemistry and climate. *Quaternary Science Reviews*, 89, 13–26,
916 doi:10.1016/j.quascirev.2014.01.019.
- 917 Hendry, K. R., Gong, X., Knorr, G., Pike, J., and Hall, I. R., (2016). Deglacial
918 diatom production in the tropical North Atlantic driven by enhanced
919 silic acid supply. *Earth and Planetary Science Letters*, 438, 122–129,
920 doi:10.1016/j.epsl.2016.01.016.
- 921 Hendry, K. R., Robinson, L. F., Meredith, M. P., Mulitza, S., Chiessi, C. M.,
922 and Arz, H., (2012). Abrupt changes in high-latitude nutrient supply
923 to the Atlantic during the last glacial cycle. *Geology*, 40, 2, 123–126,
924 doi:10.1130/G32779.1.
- 925 Holzer, M., and Brzezinski, M. A., (2016). Controls on the silicon isotope distri-
926 bution in the ocean: New diagnostics from a data-constrained model. *Global*
927 *Biogeochemical Cycles*, 29, 267–287, doi:10.1002/2014GB004967.
- 928 Horn, M., Beucher, C. P., Robinson, R. S., and Brzezinski, M. A., (2011). Southern
929 ocean nitrogen and silicon dynamics during the last deglaciation. *Earth and*
930 *Planetary Science Letters* 310, 334–339, doi:10.1016/j.epsl.2011.08.016.
- 931 Hülse, D., Arndt, S., Wilson, J. D., Munhoven, G., and Ridgwell, A., (2017).
932 Understanding the causes and consequences of past marine carbon cy-
933 cling variability through models. *Earth-Science Reviews* 171, 349–382,
934 doi:10.1016/j.earscirev.2017.06.004.
- 935 Hutchins, D. A., and Bruland, K. W., (1998). Iron-limited diatom growth and
936 Si:N uptake ratios in a coastal upwelling regime. *Nature*, 393, 561–564,
937 doi:10.1038/31203.
- 938 Jaccard, S. L., and Galbraith, E. D., (2011). Large climate-driven changes of oceanic
939 oxygen concentrations during the last deglaciation. *Nature Geoscience*, 5, 151–
940 156, doi:10.1038/NGEO1352.
- 941 Jaccard, S. L., Galbraith, E. D., Martínez-García, A., and Anderson, R. F., (2016).
942 Covariation of deep Southern Ocean oxygenations and atmospheric CO₂
943 through the last ice age. *Nature*, 530, doi:10.1038/nature16514.
- 944 Kamatani, A., (1992). Dissolution Rates of Silica from Diatoms Decomposition at
945 Various Temperatures. *Marine Biology*, 68, 91–96.
- 946 Knutti, R., Furrer, R., Tebaldi, C., Cermak, J., and Meehl, G. A., (2009). Challenges
947 in Combining Projections from Multiple Climate Models. *Journal of Climate*,
948 2739–2758, doi:10.1175/2009JCLI3361.1.
- 949 Kohlfeld, K. E., Graham, R. M., de Boer, A. M., Sime, L. C., Wolff, E. W., Le
950 Quéré, C., and Bopp, L., (2013). Southern Hemisphere westerly wind changes
951 during the Last Glacial Maximum: paleo-data synthesis. *Quaternary Science*
952 *Reviews*, 68, 76–95, doi:10.1016/j.quascirev.2013.01.017.

- 953 Kriest, I., and Oschlies, A., (2008). On the treatment of particulate organic matter
954 sinking in large-scale models of marine biogeochemical cycles. *Biogeosciences*,
955 5, 55-72, doi:10.5194/bg-5-55-2008.
- 956 Lagarias, J. C., Reeds, J. A., Wright, M. H., and Wright, P. E., (1998). Covergence
957 Properties of the Nelder–Mead Simplex Method in Low Dimensions. *SIAM*
958 *Journal on Optimization*, 9,1,112–147, doi:10.1137/S1052623496303470.
- 959 Locarnini, R. A., Mishonov, A. V., Antonov, J. I., Boyer, T. P., Garcia, H. E., Bara-
960 nova, O. K., Zweng, M. M., and Johnson, D. R., (2010). *World Ocean Atlas*
961 2009, Volume 1: Temperature. S. Levitus, Ed. NOAA Atlas NESDIS 68, U.S.
962 Government Printing Office, Washington, D.C., 184 pp.
- 963 Löptien, U., and Dietze, H., (2015). Constraining parameters in marine pelagic
964 ecosystem models - is it actually feasible with typical observations of standing
965 stocks? *Ocean Science*, 11, 4, 573–590, doi:10.5194/os-11-573-2015.
- 966 Löptien, U., and Dietze, H., (2017). Effects of parameter indeterminacy in pelagic
967 biogeochemical modules of Earth System Models on projections into a warm-
968 ing future: The scale of the problem. *Global Biogeochemical Cycles*, 31, 7,
969 1155–1172, doi:10.1002/2017GB005690.
- 970 Löptien, U., and Dietze, H., (2019). Reciprocal bias compensation and ensuing un-
971 certainties in model-based climate projections: pelagic biogeochemistry versus
972 ocean mixing. *Biogeosciences*, 16, 1865–1881, doi:10.5194/bg-16-1865-2019.
- 973 Margo Project Members, (2009). Constraints on the magnitude and patterns of
974 ocean cooling at the Last Glacial Maximum. *Nature Geoscience*, 2, 127–132,
975 doi:10.1038/NGEO411.
- 976 Matsumoto, K., Chase, Z., and Kohfeld, K., (2014). Different mechanisms of silicic
977 acid leakage and their biogeochemical consequences. *Paleoceanography*, 29,
978 doi:10.1002/2013PA002588.
- 979 Matsumoto, K., Sarmiento, J. L., and Brzezinski, M. A., (2002). Silicic acid leak-
980 age from the Southern Ocean: A possible explanation for glacial atmospheric
981 $p\text{CO}_2$. *Global Biogeochemical Cycles*, 16, 3, 1031, doi:10.1029/2001GB001442.
- 982 Matsumoto, K., and Sarmiento, J. L., (2008). A corollary to the silic acid leakage
983 hypothesis. *Paleoceanography*, 23, PA2203, doi:10.1029/2007PA001515.
- 984 McGee, D., Broecker, W. S., and Winckler, G., (2010). Gustiness: The driver
985 of glacial dustiness? *Quaternary Science Reviews*, 29, 17-18, 2340–2350,
986 doi:10.1016/j.quascirev.2010.06.009.
- 987 Meyerink, S., Ellwood, M. J., Maher, W., and Strzepek, R., (2017). Iron Avail-
988 ability Influences Silicon Isotope Fractionation in Two Southern Ocean
989 Diatoms (*Proboscia inermis* and *Eucampia antarctica*) and a Coastal Di-
990 atom (*Thalassiosira pseudonana*). *Frontiers in Marine Science*, 4, 217,
991 doi:10.3389/fmars.2017.00217.
- 992 Moore, J. K., Fu, W., Primeau, F., Britten, G. L., Lindsay, K., Long, M., Doney,
993 S., Mahowald, N., Hoffman, F., and Randerson, J., (2018). Sustained climate
994 warming drives declining marine biological productivity. *Science*, 359, 6380,
995 1139–1143, doi:10.1126/science.aao6379.
- 996 Notz, D., (2015). How well must climate models agree with observations?
997 *Philosophical Transactions of the Royal Society A.*, 373, 20140164,
998 doi:10.1098/rsta.2014.0164.
- 999 Opfergelt, S., Burton, K. W., Pogge von Strandmann, P. A. E., Gislason, S. R.,
1000 and Halliday, A. N., (2013). Riverine silicon isotope variations in glaciated
1001 basaltic terrains: Implications for the Si delivery to the ocean over glacial-
1002 interglacial intervals. *Earth and Planetary Science Letters*, 369–370, 211–219,
1003 doi:10.1016/j.epsl.2013.03.025.
- 1004 Peltier, W. R. (1994). Ice age paleotopography. *Science*, 265(5169), 195-201,
1005 doi:10.1126/science.265.5169.195.
- 1006 Pichevin, L. E., Reynolds, B. C., Ganeshram, R. S., Cacho, I., Pena, L., Keefe,
1007 K., and Ellam, R. M., (2009). Enhanced carbon pump inferred from relax-

- 1008 ation of nutrient limitation in the glacial ocean. *Nature*, 459, 1114–1117,
1009 doi:10.1038/nature08101.
- 1010 Pondaven, P., Ruiz-Pino, D., Fravallo, C., Tréguer, P., and Jeandel, C., (2000). In-
1011 terannual variability of *Si* and *N* cycles at the time-series station KERFIX
1012 between 1990 and 1995 - a 1-D modelling study. *Deep Sea Research I*, 47,
1013 223–257, doi:10.1016/S0967-0637(99)00053-9.
- 1014 Ragueneau, O., Tréguer, P., Leynaert, A., Anderson, R. F., Brzezinski, M. A., De-
1015 Master, D. J., Dugdale, R. C., Dymond, J., Fischer, G., François, R., Heinze,
1016 C., Maier-Reimer, E., Martin-Jézéquel, V., Nelson, D. M., and Quéguiner,
1017 B., (2000). A review of the Si cycle in the modern ocean: recent progress
1018 and missing gaps in the application of biogenic opal as a paleoproductiv-
1019 ity proxy. *Global and Planetary Change*, 26, 4, 317–365, doi:10.1016/S0921-
1020 8181(00)00052-7.
- 1021 Rahman, S., Aller, R. C., and Cochran, J. K., (2017). The Missing Silica Sink:
1022 Revisiting the Marine Sedimentary Si Cycle Using Cosmogenic ³²Si. *Global*
1023 *Biogeochemical Cycles*, 31, 1559–1578, doi:10.1002/2017GB005746.
- 1024 Reynolds, B. C., (2009). Modeling the modern marine $\delta^{30}\text{Si}$ distribution. *Global*
1025 *Biogeochemical Cycles*, 23, GB2015, doi:10.1029/2008GB003266.
- 1026 Reynolds, B. C., Frank, M., and Halliday, A. N., (2006). Silicon isotope fractionation
1027 during nutrient utilization in the North Pacific. *Earth and Planetary Science*
1028 *Letters*, 244, 431–443, doi:10.1016/j.epsl.2006.02.002.
- 1029 Richter, F. M., and Turekian, K. K., (1993). Simple models for the geochemical
1030 response of the ocean to climatic and tectonic forcing. *Earth and Planetary*
1031 *Science Letters*, 119, 1-2, 121–131, doi:10.1016/0012-821X(93)90010-7.
- 1032 Rosenthal, Y., Boyle, E. A., and Labeyrie, L., (1997). Last glacial maximum
1033 paleochemistry and deepwater circulation in the Southern Ocean: Ev-
1034 idence from foraminiferal cadmium. *Paleoceanography*, 12, 6, 787–796,
1035 doi:10.1029/97PA02508.
- 1036 Schoelynck, J., Subalusky, A. L., Struyf, E., Dutton, C. L., Unzué-Belmonte, D.,
1037 Van de Vijver, B., Post, D. M., Rosi, E. J., Meire, P., and Frings, P., (2019).
1038 Hippos (*Hippopotamus amphibius*): The animal silicon pump. *Science Ad-*
1039 *vances*, 5, 5 1–10, doi:10.1126/sciadv.aav0395 .
- 1040 Sime, L. C., Kohfeld, K. E., Le Quééré, Wolff, E. W., de Boer, A. M., Graham,
1041 R. M., and Bopp, L., (2013). Southern Hemisphere westerly wind changes
1042 during the Last Glacial Maximum: model-data comparison. *Quaternary Sci-*
1043 *ence Reviews*, 64, 104–120, doi:10.1016/j.quascirev.2012.12.008.
- 1044 Stoll, H., (2020). 30 years of the iron hypothesis of ice ages. *Nature*, 578, 370–371,
1045 doi:10.1038/d41586-020-00393-x.
- 1046 Sutton, J. N., Varela, D. E., Brzezinski, M. A., and Beucher, C. P., (2013). Species-
1047 dependent silicon isotope fractionation by marine diatoms. *Geochimica et Cos-*
1048 *mochimica Acta*, 104, 300-309, doi:10.1016/j.gca.2012.10.057.
- 1049 Sutton, J. N., André, L., Cardinal, D., Conley, D. J., de Souza, G. F., Dean, J.,
1050 Dodd, J., Ehlert, C., Ellwood, M. J., Frings, P. J., Grasse, P., Hendry, K.,
1051 Leng, M. J., Michalopoulos, P., Panizzo, V. N., and Swann, G. E. A., (2018).
1052 A Review of the Stable Isotope Bio-geochemistry of the Global Silicon Cy-
1053 cle and Its Associated Trace Elements, *Frontiers in Earth Science*, 5, 112,
1054 doi:10.3389/feart.2017.00112.
- 1055 Tréguer, P., Nelson, D. N., Van Bennekom, A. J., DeMaster, D. J., Leynaert, A.,
1056 and Quéguiner, B., (1995). The Silica Balance in the World Ocean: A Reesti-
1057 mate. *Science*, 268, 5209, 375–379, doi:10.1126/science.268.5209.375 .
- 1058 Tréguer, P. J., and De La Rocha, C. L., (2013). The World Ocean Silica Cycle.
1059 *Annual Review of Marine Science*, 5, 477–501, doi:10.1146/annurev-marine-
1060 121211-172346.
- 1061 Weaver, A. J., Eby, M., Wiebe, E. C., Bitz, C. M., Duffy, P. B., Ewen, T. L., Fan-
1062 ning, A. F., Holland, M. M., Macfadyen, A., Matthews, H. D., Meissner, K. J.,

- 1063 Saenko, O., Schmittner, A., Wang, H., and Yoshimori, M., (2001). The UVic
1064 Earth System Climate Model: Model description, climatology, and applica-
1065 tions to past, present and future climates. *Atmosphere-Ocean*, 39, 361–428,
1066 doi:10.1080/07055900.2001.9649686.
- 1067 Wischmeyer, A. G., De La Rocha, C., Maier-Reimer, E., and Wolf-Gladrow, D. A.,
1068 (2003). Control mechanisms for the oceanic distribution of silicon isotopes.
1069 *Global Biogeochemical Cycles*, 17, 3, 1083, doi:10.1029/2002GB002022.